Biologically Inspired Underwater Propulsion and Adhesion Mechanisms

by

Yichao Pan

B.S., University of Notre Dame (2012)

Submitted to the Department of Mechanical Engineering
in Partial Fulfillment of the Requirements for the Degree of

Master of Science in Mechanical Engineering

at the

MASSACHUSETTS INSTITUTE OF TECHNOLOGY

September 2014

Signature redacted

Signature of Author .....
Department of Mechanical Engineering
August 8, 2014

Signature redacted

Certified by .....
Sangbae Kim
Assistant Professor of Mechanical Engineering
Thesis Supervisor

Signature redacted

Accepted by .....
David E. Hardt
Chairman, Department Committee on Graduate Theses

Biologically Inspired Underwater Propulsion and Adhesion Mechanisms

by

Yichao Pan

Submitted to the Department of Mechanical Engineering
on August 8, 2014, in Partial Fulfillment of the Requirements for the Degree of
Master of Science in Mechanical Engineering

Abstract

The ultimate objective of this research is to develop an innovative underwater pipe inspection robot with both swimming and crawling capabilities as opposed to conventional in-pipe robots with wheeled designs or driven by propellers. The contents of this thesis include two different parts: a propulsion mechanism using a passive compliant tail and a reversible underwater adhesion mechanism.

The propulsion mechanism is the primary concern of this research. The hypothesis of this part of research is that a continuous passive compliant tail structure with an optimized stiffness profile in its longitudinal direction along with the proper control of a single actuator can allow the undulatory motion of this mechanism to resemble real fish swimming locomotion. This approach is in contrast to conventional approaches where multiple joints are actuated to create traveling waves to emulate propulsion mechanisms of fish. Four iterations of experiments are developed in total to verify the hypothesis, take measurements and improve the performance of the propulsion mechanism. It is proven that a continuous passive compliant structure driven by a DC motor through a four bar linkage can generate sufficient propulsion to drive a moving unit forward along a guide rail. The experiments with a simple prototype demonstrate that the propulsion mechanism is promising to drive a robot forward along a prescribed path without a guide rail. It is demonstrated that the stiffness profile in the longitudinal direction is one of the critical factors that affects the performance of the propulsion mechanism. A simulation model is developed to guide the design process of the passive compliant structure, mainly to optimize its stiffness profile along the tail structure. Special measures are implemented into the experiments to extract data to compare with simulated results.

The reversible underwater adhesion mechanism is another critical component of the underwater pipe inspection robot that is under development. The goal of developing a reversible underwater adhesion mechanism is to provide adequate traction to various surfaces while the robot operates in water. This reversible underwater adhesion mechanism allows a robot to stick and crawl in water pipes even across the stream. This mechanism may enable recharging capability extracting energy from kinetic energy of the pipe flow.

Two generations of robot prototypes are developed to demonstrate the crawling and propulsion mechanisms.

Thesis Supervisor: Sangbae Kim
Title: Assistant Professor of Mechanical Engineering

This page intentionally left blank.

Acknowledgments

First of all, I would like to express my gratitude to my supervisor, Dr. Sangbae Kim, whose expertise, understanding, and patience, added considerably to my graduate experience. He guided me through this research with his vast knowledge and skills in the field of robotics and mechanical design. I greatly appreciate the opportunity that he offered me to join his research group to learn more about robotics, which is a fascinating topic that I will keep following in my life.

I would like to thank Dr. Sami Habib at Kuwait University, who initiated this research and collaborated with our group diligently. I sincerely appreciate the generous support from the Kuwait-MIT Center for Natural Resources and the Environment, where the research funding came from.

I would like to thank all my fellow labmates in the MIT Biomimetic Robotics Lab: Albert Wang, Michael Chuah, Matt Haberland, Haewon Park, Sangin Park, João Luiz Ramos and Will Bosworth. I would not be able to finish my research without their consistent support and valuable suggestions.

I would especially like to thank Dr. Franz Hover, who generously allowed me to set up the experiments in the testing pool in his lab. I also appreciate the help I received from Eric Gilbertson while doing experiments there.

My sincere thanks also go to Dr. Peko Hosoi, who provided great support to this research project. I would like to thank Dr. Lisa Burton and Josh Wiens for sharing their abundant knowledge in fish swimming with me.

Last but not the least, I would like to thank my parents Fang Pan and Dongfang Shi for their tremendous support throughout my life. I would also like to thank my grandparents Zhihui Pan and Jingxian Bai, who raised me up and made me who I am today.

This page intentionally left blank.

CONTENTS

CHAPTER 1

INTRODUCTION

The ultimate objective of this research is to develop an innovative underwater pipe inspection robot with both swimming and crawling capabilities as opposed to conventional in-pipe robots with wheeled designs or driven by propellers. The contents of this thesis include two different parts: a propulsion mechanism using a passive compliant tail and a reversible underwater adhesion mechanism.

The objective of the first part of this research is to investigate the application of a passive compliant underwater propulsion mechanism in the design of a fast swimming robot with high energy efficiency. This mechanism consists of one electric motor which enables undulatory motion of a slender and flexible structure with an optimized stiffness profile in the longitudinal direction similar to the body of an eel or lamprey.

Roboticists have been studying the compliance of legged robots, but so far there has been rarely any research on the role of compliance in swimming robots. Fish locomotion has been a long-lasting active research topic ever since 1930s. Biologists, mathematicians and roboticists have observed, investigated and categorized different modes of fish locomotion and developed a variety of theories and models to describe them. The diversity in body motions and anatomies and the complexity of hydrodynamic interactions prevent researchers from generating a simple and precise model to describe fish locomotion. A common approach taken by roboticists is to prescribe a kinematic configuration for a fish robot to follow by applying suitable control techniques to the actuators [1][2][3]. The kinematic equation is usually derived based on the observation of real fish and has a limited number of tunable parameters. Such fish robots generally have multiple discrete segments and actuators, thus having a restricted number of degrees of freedom. The dynamic interaction of the undulatory body with the surrounding water is too complex to model and often ignored in this kinematic approach.

In this research, a continuous passive compliant mechanism is adopted to replace the common mechanism with discrete segments. With only one actuator, the energy efficiency is expected to be superior to that of existing swimming robots with multiple actuators. An optimized stiffness profile in the longitudinal direction along with the proper control of the single actuator

allows the undulatory motion of this mechanism to resemble real fish swimming locomotion. The mechanism is back drivable due to its compliance, hence adapting to the surrounding liquid more easily. The robot is designed to swim fast while maintaining high energy efficiency.

A MATLAB simulation of the mechanism is generated based on the Lagrangian approach. The typical hydrodynamic forces, such as drag and added-mass forces, are taken into account in the model, which can be used to obtain desired local material properties, in particular, stiffness. The aim of this simulation is to provide general insights to guide the design process of a swimming robot. Meanwhile, a series of experiments are conducted to verify the simulated results until an acceptable solution is found based on the design criteria.

Ideally, the intended mechanism should be modeled continuous, though it is considerably challenging to achieve this. It is worth to emphasize that our goal is not to build a highly precise model but rather to learn some general insights about this type of underwater flexible mechanism, especially its interaction with surrounding water. Therefore, the mechanism is modeled as a series of 2D rigid segments connected by pin joints with tunable stiffness. By increasing the number of segments and decreasing their lengths, this model can approach the continuous model. The stiffness of each joint can be optimized to achieve the maximum steady-state velocity of this mechanism. A prototype can thus be constructed based on this optimized stiffness profile.

Several iterations of experiments have been developed to verify the hypothesis and generate more insights to guide the design process. The passive compliant structure is molded with polyurethane with suitable elasticity. A DC motor is selected as the single actuator, and its continuous rotation is translated to oscillation through a four bar linkage. The propulsion mechanism is tested along a guide rail under water. A quick experiment off the guide rail proves that such a propulsion mechanism is promising to drive a robot forward along a prescribed path.

The objective of the second part of this research is to develop a reversible underwater adhesion mechanism. The pipe inspection robots developed recently use a range of different locomotion strategies, among which a combination of wheels and legs is the most common method. In-pipe wheeled robots apply a normal force against the pipe walls to maintain traction and gain propulsion by rotating the wheels [4]. The wheels are typically connected to and controlled by legs in a linkage mechanism with springs that generates a constant normal force, thus resulting in constant friction provided that the interior pipe diameter and surface roughness remains the same. A recent design uses a novel mechanism with permanent magnets to generate a variable normal

force to avoid unnecessary high friction and reduce the energy loss [5]. Most in-pipe wheeled robots adapt a design that includes three pairs of wheels 120 degrees apart in the cross-section view to support the robot body at the center of the pipe [6][7][8][9].

Most wheeled robots can only fit in a specified pipe size [6][7], while few models can operate within a limited range of varied pipe diameters [8]. The lack of adaptability to different pipe diameters and large cross-sections relative to the pipe interior greatly restrict the operation range of in-pipe wheeled robots. Another imposing challenge for in-pipe robots is power supply. A number of robots are self-contained with embedded batteries [6], but many other wheeled robots, including commercial models [9][10], are commonly tethered to external power supplies outside the pipe, which allows extended working hours and more embedded electric devices while restricting the operation range by the tether length [7][8]. Nevertheless, in-pipe wheeled robots generally can maintain sufficient traction and some existing models have the ability to maneuver through up to 90-degree turns, climb up a slope, or even crawl up vertically.

To overcome the limitations of wheeled design, a reversible underwater adhesion mechanism is designed to generate tractions for underwater robots. A micro active suction cup array (MASCA) actuated by a liquid pump is developed to demonstrate its feasibility of accomplishing reversible underwater adhesion.

Two generations of robot prototypes have been developed to demonstrate the crawling and propulsion mechanisms.

CHAPTER 2

SIMULATION OF PROPULSION MECHANISM

In order to guide the design of the propulsion system, a reasonably accurate simulation is desirable. Ideally the simulation is expected to predict an optimized stiffness profile that enables the design of a fast propulsion system while achieving high efficiency. In practice, simulation can never predict reality precisely. Therefore, the simulation is expected to show at least a general relationship between the stiffness profile and the corresponding swimming speed at different energy input levels. The error should be reduced as much as possible to improve the quality of the simulation. In this section, the theory that the simulation is based upon, the MATLAB scripts that have been used, and the preliminary results are discussed in detail.

2.1 LAGRANGIAN FORMULATION

In order to simulate the passive compliant underwater propulsion system, the first question that should be considered is how to model it. In reality the system is continuous with various stiffness along the longitudinal direction. To avoid using complicated differential equations to describe this system, the whole system is discretized into multiple rigid links connected by pin joints with adjustable stiffness. One of these joints is driven by an actuator. By increasing the number of links and decreasing their lengths, the multi-link model approaches to a continuous one. Furthermore, the model is assumed to be two dimensional. Thus, the problem has been simplified considerably to how to simulate a 2D multi-link rigid body system, which is a common type of mechanism to model.

The second question is how to obtain the equations of motion of such a system. The dynamic behavior is described in terms of the time rate of change of the mechanism configuration in relation to the joint torques exerted by the actuators. This relationship can be described by the equations of motion that govern the dynamic response of the links to input joint torques.

In general, two methods can be used to obtain the equations of motion: the Newton-Euler formulation, and the Lagrangian formulation. The Newton-Euler formulation is derived by the direct interpretation of Newton's Second Law of Motion, which describes dynamic systems in terms of force and momentum. The equations incorporate all the forces and moments acting on the

individual links, including the coupling forces and moments between the links. The equations obtained from the Newton-Euler method include the constraint forces acting between adjacent links. Thus, additional arithmetic operations are required to eliminate these terms and obtain explicit relations between the joint torques and the resultant motion in terms of joint displacements.

In the Lagrangian formulation, on the other hand, the system's dynamic behavior is described in terms of work and energy using generalized coordinates. Therefore, all the workless forces and constraint forces and constraint forces are automatically eliminated in this method. The resultant equations are generally compact and provide a closed-form expression in terms of joint torques and joint displacements. Furthermore, the derivation is simpler and more systematic than in the Newton-Euler method [11].

When the system contains a small number of links, it is possible to use either formulation to derive the equations of motion. However, when the number of links increases, the Newton-Euler formulation requires tremendously more work than the Lagrangian formulation. In other words, the Lagrangian formulation is more scalable. Since the dynamic response of the system is the primary concern instead of the constraint forces, the Lagrangian formulation is feasible to solve the problem.

In the Lagrangian formulation, the m^{th} ($m = 1, \ldots, n$) equation of motion is given by

$$\frac{d}{dt}\frac{\partial L}{\partial \dot{q}_m} - \frac{\partial L}{\partial q_m} = Q_m, \tag{2-1}$$

where L is the Lagrangian, which equals $T - V$. T is the kinetic energy, and V is the potential energy. q_m is the m^{th} generalized coordinate, and Q_m is the m^{th} generalized force.

2.2 ALGORITHM

Dr. Matthew Haberland in the MIT Biomimetic Robotics Lab developed a set of algorithms in MATLAB to derive the equations of motion systematically using the Lagrangian formulation. The set of algorithms has been modified extensively to serve the purpose of this project.

A few critical assumptions are made for the simulation:

- The tail structure is simulated as a 2D model for simplicity. The entire structure has infinite depth perpendicular to the 2D surface where the model is in. The thickness of each link is neglected, so the links are only varied by length.
- The continuous tail structure is approximated by a number of discrete rigid links, which are connected by joints with tunable stiffness. Increasing the number of links can improve the accuracy of the model, but it also makes the simulation more computationally demanding.
- The hydrodynamic forces that are considered in the simulation include only the friction and form drags and the added-mass forces. The friction drag acts parallel along each link, whereas the form drag acts perpendicular to each link. The expressions of the added-mass forces are derived based on a 2D narrow rectangular model.
- The hydrodynamic forces are applied to the individual links separately. In reality the hydrodynamic forces may be altered by interactions between the links, but this effect is neglected in the simulation. The links are almost independent to each other with interactions at the joints only. Turbulence is not considered in the simulation either because it is challenging to model in a simple way.

The set of algorithms contain two primary MATLAB files. The first file, derive_EoM.m, is used to derive the equations of motion symbolically. A set of MATLAB functions is generated automatically after running this file. The second file, simulate.m, is used to solve the equations of motion with numeric values of the variables involved in the equations. This file also calls a function, animation.m, to visualize the simulation in the form of an animation.

The equations of motion are derived by derive_EoM.m. Appendix A contains the MATLAB script.

The two variables, *dim* and *pts*, are defined at the very beginning of this file: *dim* defines the number of links in the simulation, and *pts* defines the number of sample points along each link. The hydrodynamic forces acting on the links are calculated only at these particular sample points. These two variables make the simulation scalable. Ideally, both variables should be as large as possible in order to approach a real continuous system, but the computation becomes increasingly challenging if these two variables are large.

The number of degrees of freedom is determined by the variable *dim*. Besides the joint angles, there are two additional degrees of freedom, x and y, which indicate the horizontal and vertical positions of the origin of the first link, respectively. The linear and angular velocities and accelerations are defined.

A set of parameters that govern the geometric and inertial properties of each link are defined, for example, the center of mass, length, moment of inertia, and neutral position. The stiffness of each joint, density of water, drag coefficients and torque input are defined as well.

The generalized coordinates q, velocities dq, and accelerations ddq are defined based on x, y, and the joint angles.

A set of fundamental vectors are defined: *ihat*, *jhat* and *khat*, which determine the x, y and z directions with respect to the fixed coordinate system. The vector *er* contains the directions along each link, and the vector *ern* contains the directions perpendicular to each link.

The beginning and end points of the links are defined as *pos*. The midpoint of each link is defined as *posM*. The positions of sample points along each link is defined as *posX*. The velocities and accelerations corresponding to these points are defined subsequently.

The kinetic and potential energies of each link are defined as T and Ve, respectively. The power of each link is defined as P.

The hydrodynamic forces acting on each link are mainly the friction drag parallel to the link, defined as Fx, and the form drag and added-mass forces perpendicular to each link, together defined as Fy.

The generalized forces are defined as *Q_tau* and *Q_F*, where *Q_tau* is due to external torques and *Q_F* is due to external forces. For this project, *Q_tau* is only due to the torque input at one selected joint.

R contains the key points that are used to generate the animation. It also defines the relative sequence of these points.

There are three anonymous functions defined in this algorithm: *ddt*, *F2Q* and *M2Q*. *ddt* is a function for taking time derivatives. *F2Q* and *M2Q* calculate the force and moment contributions to the generalized forces.

After all the variable are initiated, the variables are represented in terms of the parameters and generalized coordinates using a loop. The hydrodynamic forces are generated using a function

HydroForce.m, presented in Appendix B. The friction drag that is parallel to each link is calculated by

$$F_x = -\frac{1}{2}\rho C_{d2} v_x |v_x| l \,, \tag{2-2}$$

where ρ is the density of water, C_{d2} is the drag coefficient in the direction parallel to the link, and v_x is the velocity of water parallel to the link. The sum of form drag and added-mass force that are perpendicular to each link is calculated by

$$F_y = -\frac{1}{2}\rho C_{d1} v_y |v_y| l - \frac{1}{2}\rho \pi l a_y \,, \tag{2-3}$$

where C_{d1} is the drag coefficient in the direction perpendicular to the link, v_y is the velocity of water perpendicular to the link, and a_y is the acceleration of water perpendicular to the link.

After the variables are defined symbolically, the equations of motion are generated. This file generates a number of functions for simulate.m to call.

The simulate.m file, presented in Appendix C, contains the numeric values of the parameters defined in derive_EoM.m. These values can be easily adjusted in order to change the configuration of the mechanism.

After the parameters are given certain numeric values, the file uses *ode45* to solve the equations of motion with the defined torque input. The equations of motion are called in the function dynamics.m, presented in Appendix D, which also contains the definition of the torque input.

The solution is input into animate.m function to generate the animation of the simulation.

2.3 PRELIMINARY RESULT

A few simulations with various parameters and number of links have been generated using this set of algorithms. Figure 1-1 shows the screenshots from the animation of one of the simulations. In this case the first link is twice as long as the following links. The actuator is located at the joint between the first and second links, where the torque is applied. The mass of the first link is larger compared to those of the following links.

The simulations verify the idea that such a mechanism driven by one actuator is able to propel itself forward in water. The remaining questions is, how to optimize the stiffness profile in the longitudinal direction.

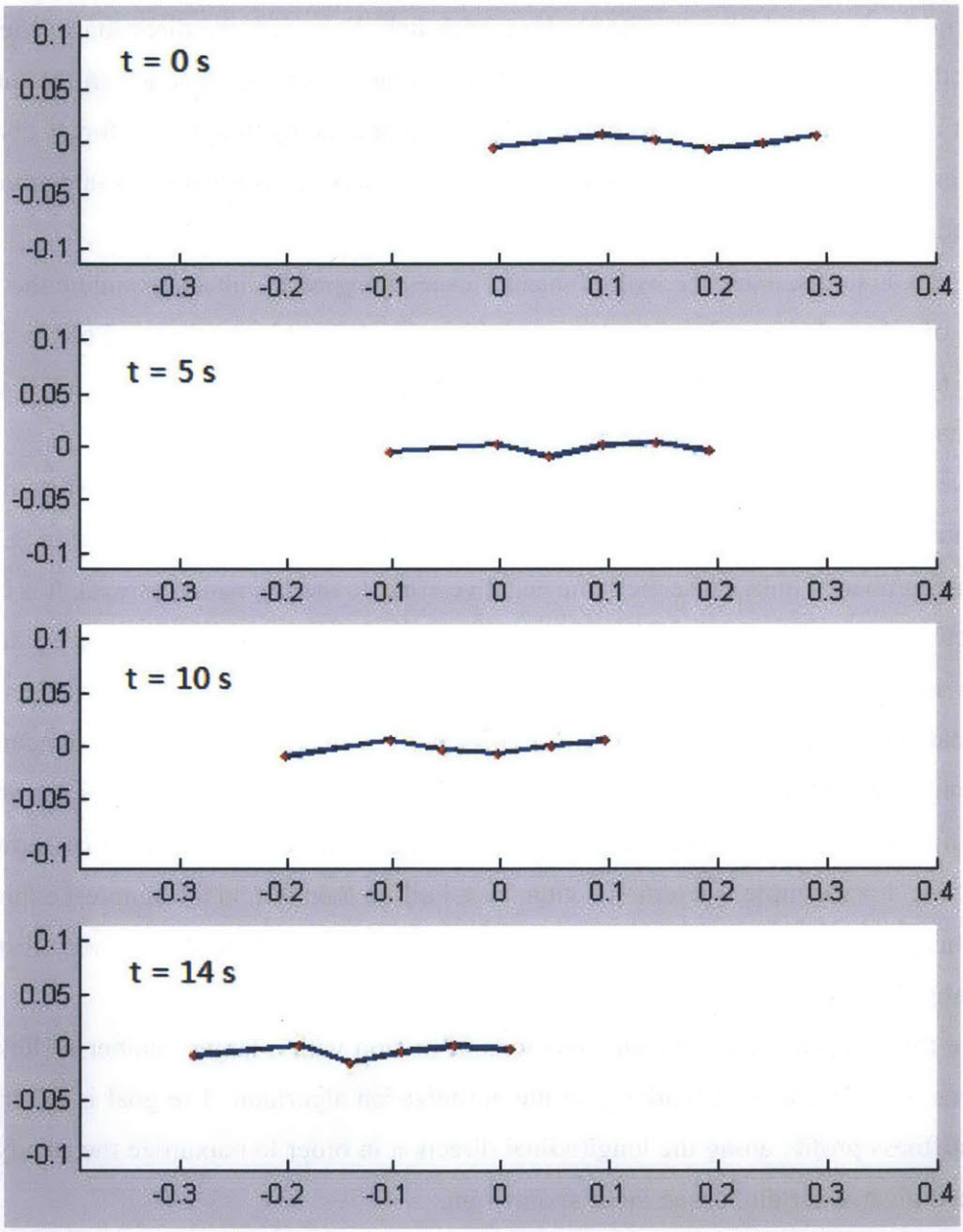

Figure 1-1. Screenshots of a Sample Simulation

2.4 DISCUSSION AND NEXT STEPS

It took a long time to set up the algorithms in a reasonable way. The major trouble that was encountered is how to calculate the hydrodynamic forces along the links. Ideally, the hydrodynamic forces should be integrated along each link. However, the direction of the force needs to be determined, which requires the use of either an *abs* or *sign* function in the integral. Somehow it is exceedingly difficult to find a way to integrate the hydrodynamic forces correctly to yield a reasonable simulation. Thus, an alternative way that is not as accurate as integration has to be adopted.

The idea is to discretize the hydrodynamic forces along each link and estimate the forces at a number of selected points. That is why a variable *pts* is defined in the derive_EoM.m file. At each point, the direction and magnitude of the forces can be determined easily, so it is less computationally demanding compared to the integration method.

However, since the forces are expressed symbolically in the derive_EoM.m file, an increasing number of sample points makes the computation significantly more challenging. Also, an increasing number of links cause the same negative effect to the simulation as well. It is critical to find a method to simplify the computation such that it takes less time to derive the equation of motion. An intuitive method is to run the algorithm on a computer or server that has more computational power. Though MATLAB can convert files into C or other more fundamental computer languages in some cases to save the computing time, the symbolic toolbox has no such support at this point. A few unnecessary steps in the algorithm are taken out to cut down the computing time. For example, *simplify* function has a built-in loop to find the simplest expression of a symbolic term, which in general takes a long time to run. This function has very restricted uses in the algorithm.

Once the algorithm can generate equations of motion with a larger number of links and sample points, it is time to start working on the optimization algorithm. The goal is to attain an optimized stiffness profile along the longitudinal direction in order to maximize the steady-state forward speed given a certain torque input at one joint.

While working on the computer simulation, a series of prototypes are constructed to gain more insights experimentally.

CHAPTER 3

FIRST ITERATION OF EXPERIMENTS

After the simulation is constructed and started generating preliminary results, it is necessary to verify the results with experimental data. Experiments are also needed to tune the key parameters in the simulation, for example, the drag coefficients. More insights can be drawn from experiments to improve the design of the simulation. The primary objective of this research is to create a fast swimming robot with high energy efficiency. Therefore it is important to start designing the robot, at least the propulsion system, before the simulation can yield useful results.

3.1 PROOF OF CONCEPT

The overall hypothesis of this research is that a continuous passive compliant structure with an optimized stiffness profile in its longitudinal direction along with the proper control of a single actuator can allow the undulatory motion of this mechanism to resemble real fish swimming locomotion. The conventional approach of building a fish robot is to install a series of servo motors along the tail. Thus the tail would have multiple joints and discrete segments. The advantage of this approach is that the joint angles can be controlled precisely so that the overall shape of the tail at each time step will follow a desired trajectory, which is often extracted from experimental data based on extensive observations of real fish. However, it is not intuitive if a passive compliant structure driven by one single actuator is sufficient to generate propulsion to drive a robot forward. This is the fundamental layer of the overall hypothesis that needs to be verified. Once this part is verified by experiments, it can be investigated whether or not optimizing the stiffness profile would allow the propulsion mechanism to generate locomotion similar to real fish. Therefore, the first step of conducting the experiment is to design a simple mechanism to prove that a passive compliant structure driven by one single actuator is able to generate propulsion forward.

A preliminary experiment is performed to prove the concept. The experiment set up is illustrated in Figure 3-1 (1). The tail is made of Ecoflex® Supersoft 0030 (Smooth-on, Inc), which is flexible and neutrally buoyant in water. The tail is connected to a rod which rotates around the axis of the servo. The servo horn is inserted into the top section of the rotating rod to ensure firm connection between the servo and rod. The servo and rod are held together by the case. The servo

is controlled and powered by an Arduino Nano board, which is not shown in the figure. The case is connected to a six-axis force sensor by a metal rod along the servo's rotating axis. The force sensor is used to measure the propulsive force generated by the tail motion. LabVIEW DAQ (National Instruments Corporation) is used to acquire the experimental data. The servo is commanded to rotate back and forth periodically with respect to its neutral position. The amplitude is defined as the largest angle away from the neutral position in a view from the top. The frequency is controlled by how fast the servo changes the rotating direction. Both amplitude and frequency are variables in the experiment.

Figure 3-1 (2) shows the side view of the tail in a stable condition under water when it is not actuated. The material is neutrally buoyant in water. Though the tail is not able to support its own weight in air due to its outstanding flexibility, it nevertheless maintains its shape well under water due to buoyancy.

Several sets of experiment are performed by varying the amplitude and frequency. Figure 3-1 (3) contains a few pictures taken in real time when the tail is driven by the servo under water. The tail is able to generate expected motions. The cross section of the tail tends to be thinner toward the end, so it seems floppy compared to the front part of the tail.

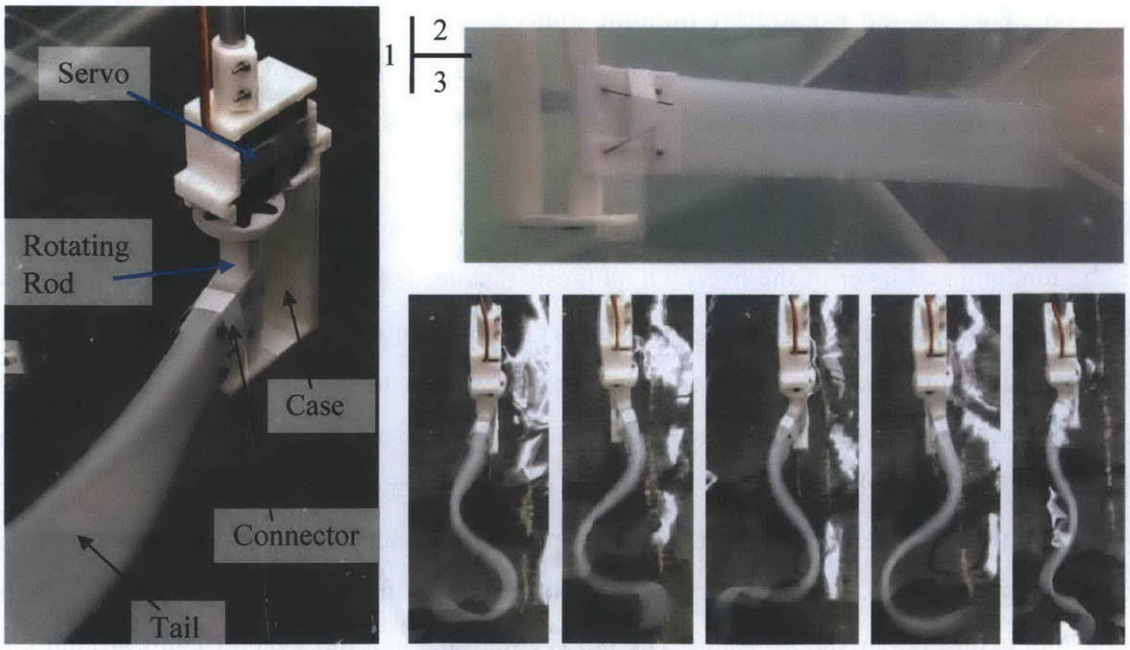

Figure 3-1. Proof-of-Concept Experiment on a Simple Tail Mechanism

Figure 3-2 demonstrates the experimental results. Each color corresponds to a distinct value of amplitude. The delay time controls how fast the servo changes its rotating direction. For example, when the tail is rotated from the left end to the right end, it delays a certain number of seconds before being rotated back. The angle is measured with respect to the neutral position.

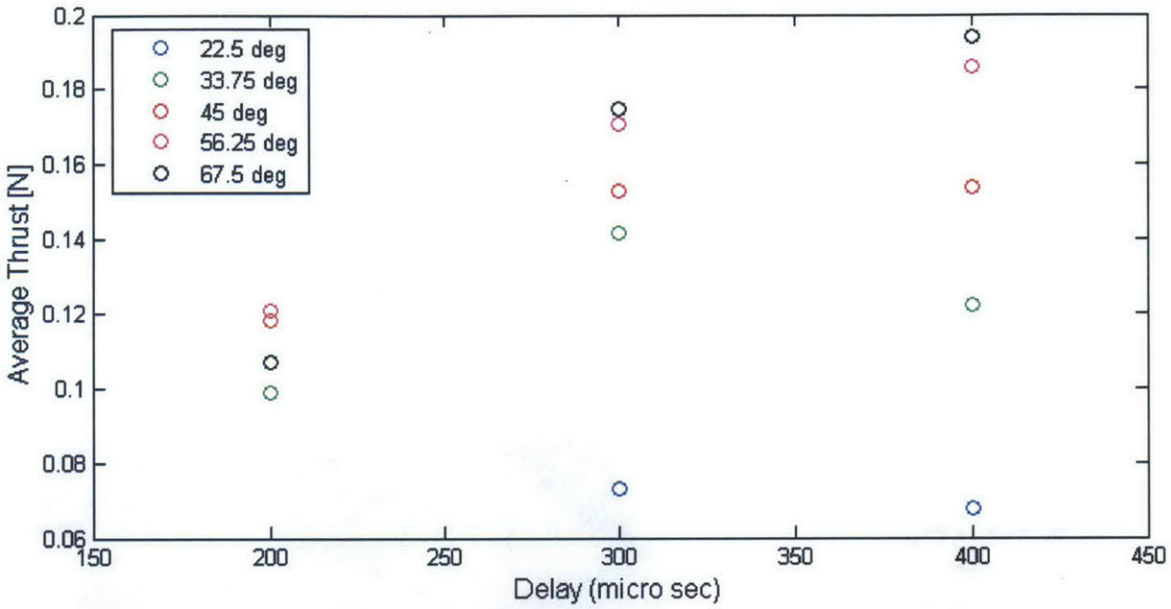

Figure 3-2. Proof-of-Concept Experimental Results (Thrust Measurement)

When the amplitude is relatively low (not greater than 45 degrees), the maximum thrust occurs at a moderate value of delay time (300 micro seconds). When the amplitude becomes larger (greater than 45 degrees), the thrust increases along with the increasing delay time. When the delay time remains constant, the thrust increases when the amplitude is greater. The only exception is when the amplitude equal to 67.5 degrees and the delay time equal to 200 micro seconds. In this case, the thrust is not the maximum compared to other data points with the same delay time. It is noticed that the servo does not reach the desired amplitude when the delay time is short (200 micro seconds). Further investigation is needed to understand this unexpected behavior of the servo.

The maximum thrust is 0.195 N, which occurs at the maximum value of both amplitude and delay time. This value seems small. It is suspected that the tail is too flexible to generate considerable propulsion. A stiffer tail may produce larger thrust. In addition, the desired motion

of the tail is unknown. The variables in this experiment are set based on intuition. More research should be done on the desired trajectory of the tail before generating commands for the servo. Nevertheless, the experiment assures that a servo can potentially drive the tail to follow a desired locomotion.

3.2 PRELIMINARY DESIGN

The tail beating frequency is mostly constrained by the servo motor in the proof-of-concept experiment. It would be ideal to drive the tail with a conventional DC motor whose speed can be controlled easily by adjusting the voltage input. A preliminary design with a DC motor as the actuator is introduced in this section. To keep the experiment simple, the motion of the whole mechanism is constrained by a guide rail so that it can only move forward or backward along a straight line. Figure 3-3 illustrates the design of the mechanism as well as the prototype constructed based on the CAD model. The guide rail is not shown in the figure.

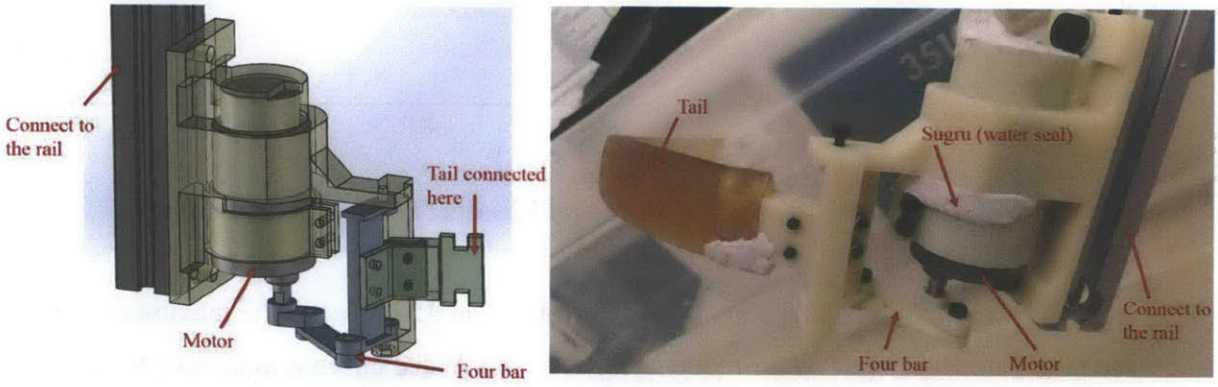

Figure 3-3. The CAD Model and the Prototype of the Preliminary Design

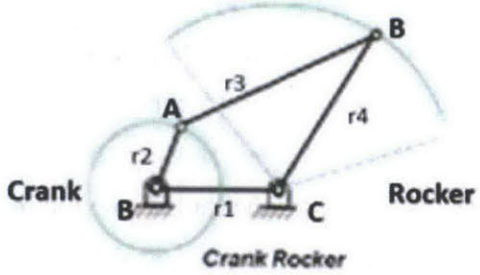

Figure 3-4. Crank-Rocker Mechanism [12]

Though it is intended to design a mechanism to verify the hypothesis quickly, it is not intuitive how to generate the undulatory motion in the soft tail made of rubber using a rotary motor. The key in this design is how to translate the rotation of motor into oscillation at the beginning of the tail with respect to an axis. In this design, a crank-rocker mechanism, one type of the four bar linkages, is adopted to achieve this function. Figure 3-4 illustrates a typical crank-rocker mechanism. A crank-rocker mechanism satisfies the condition that $r1+r2 < r3+r4$. The crank can rotate 360 degrees continuously, while the rocker can only rotate through a limited range of angles.

Typically a four bar linkage is planar, but in this design the crank-rocker mechanism is modified into a 3D version to accomplish the goal. The crank is directly connected to the shaft of the motor so that it can be driven continuously along with the motor shaft. The rocker is the purple piece that is connected to the green piece, which is a 3D printed plastic piece molded into the soft rubber tail. The purple piece that connects the crank and rocker functions as the coupler ($r3$ in Figure 3-4). The ground ($r1$ in Figure 3-4) is integrated into the motor housing. In order for the beginning of the soft tail to oscillate symmetrically with respect to the symmetric plane of the motor, the rocker has an extension that forms an angle with the rocker. If the tail were connected to the rocker directly without this extension, the range of oscillation would not be symmetric with respect to the symmetric plane of the motor. Figure 3-5 illustrates the arrangements in different views.

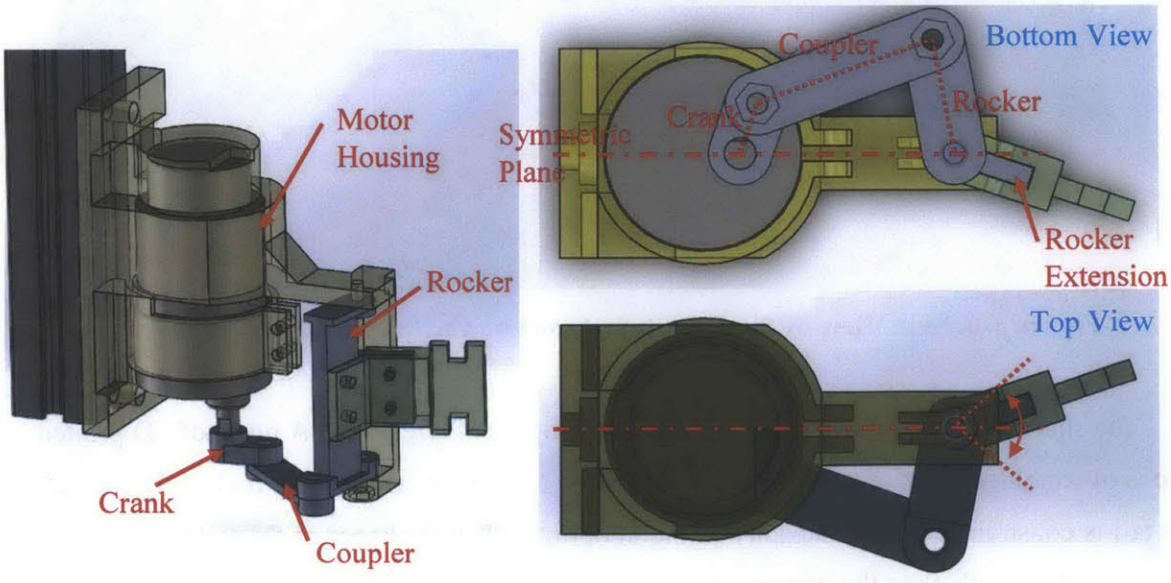

Figure 3-5. Crank-Rocker in the CAD Model

The dimensions of the crank-rocker mechanism are determined in a sketch in SolidWorks. The major factors that are taken into account include the dimensions of the motor and the molded tail, which is decided to be 24 cm long. Since the tail is expected to be molded with polyurethane or silicone rubber and the molds are 3D printed using the Stratasys® Dimension printer readily available in the lab, the length of the tail is constrained by the maximum dimension of the molds that can be produced on the printer. The lengths of the rocker, coupler and crank are determined roughly based on the outer radius of the motor and the length of the tail. The range of oscillation of the extension of the rocker, which is connected directly with the beginning of the tail, is also determined based on a reasonable estimation. In short, the specific dimensions of the entire setup are not optimized with respect to any criteria to achieve high performance. Again, the goal is to set up a mechanism that can quickly verify the hypothesis that a passive compliant tail driven by one single actuator can generate propulsion that is sufficient to propel the whole system forward.

3.3 PROTOTYPE

Figure 3-6 illustrates the side view of the prototype based on the preliminary design.

Figure 3-6. Side View of the Prototype based on the Preliminary Design

The shape of the tail is designed to be similar to that of a real fish. A piece of 3D printed plastic is overmolded into the tail so that it is easier to connect the tail with the rocker. The length of the tail is constrained by the capacity of the 3D printer. The thickness of the tail varies along with the length. It is thick at the beginning and becomes thinner toward the end. The width of the

tail also varies along with the length. It first gets narrower and then wider at the end. Since the material is homogeneous except the 3D printed piece at the beginning, the stiffness is largely correlated with the local geometry. The tail is rigid at the beginning, especially the section that contains the 3D printed part, but the end of the tail is floppier compared to the rest of the tail, although the area in the side view is larger. Similar to the design of the crank-rocker mechanism, the specific dimensions of the tail are determined based on estimation rather than rigorous analysis or simulation. Eventually the design will be guided by the simulation, but there is not enough information at this stage yet, nor is it necessary to bring in the simulation for this simple setup that is used to verify the hypothesis.

In addition to the geometry, the material that is used to mold the tail also affects the stiffness significantly. The tail can neither be too rigid nor too floppy in order to create a reasonable undulatory motion that is able to generate propulsion. Based on the experience dealing with the Smooth-On® materials, mainly the EcoFlex® and VytaFlex® series, the VytaFlex® 20 is selected due to its relatively low viscosity and appropriate flexibility. The VytaFlex® 20 consists of two liquid parts that are mixed together according to 1:1 volume or weight ratio. The viscosity while the mixed material is still liquid largely affects the quality of the final product, because it needs to be put in a vacuum chamber to degas, a critical process that reduces the number of air bubbles in the final product. If the viscosity of the mixed material in the liquid state is too high, the air bubbles would be trapped in the product and mold, and the final product after sufficient solidification would be undesirably porous. VytaFlex® 40 and 60 are stiffer and more difficult to degas than VytaFlex® 20. EcoFlex® 0010 and 0030 are too flexible and easy to deform. Therefore, VytaFlex® 20 is selected to make the tail in this prototype.

The motor used as the sole actuator in this design is the 19:1 Metal Gearmotor 37Dx52L mm with 64 CPR Encoder purchased from Pololu [13]. The major advantages of using this motor include: (1) it is inexpensive, (2) it comes with an encoder attached, and (3) it is expected to deliver sufficient power to drive the tail under water. The very first concern of this experimental setup is how to make the motor waterproof so that it can operate under water. That is why the motor housing covers around the motor to avoid direct exposure to the water. Sugru® is a type of self-setting rubber that is used to enhance the waterproof capability of the setup. It is mainly applied to seal the gap between the motor and motor housing, as well as the holes on the external surface of the motor that is not covered by the motor housing. The only interface that is vulnerable to water

penetration is around the motor shaft. In order to ensure that the motor shaft can spin freely, no sugru or other sealant is applied around the shaft. The motor comes with lubrication between the shaft and the stationary part, and it is assumed that the lubrication is able to prevent water from flowing into the motor easily.

The motor is powered by an external power supply that is connected with the motor through a long wire. Ideally batteries should be carried on board in the final product. But to keep the setup simple to use without worrying about maintaining stable and sufficient power input into the system, a power supply with adjustable voltage output is adopted to power the motor. The power supply is kept away from water during the experiment to ensure safety.

The motor housing is bolted onto an aluminum extrusion which is attached to a carriage constrained on a linear guide rail. The carriage can move freely along the rail with low friction. The experiment is conducted in a plastic storage container that is roughly 50 cm long, 35 cm wide and 40 cm tall. The water level is about 20 cm above the bottom of the container, and the motor and tail assembly is entirely submerged under water. The guide rail is positioned right above the container and sits on its top edges. The motor is intended to operate at 12 V, but it can start rotate when the voltage is as low as 1 V. Since the motor operates under water, the problem of overheating is less of a concern. The voltage input ranges between 1 V up to 25 V during the experiment, and the motor speed does not seem to saturate yet. A video of the experiment is available on YouTube [14]. A screenshot of the video is shown in Figure 3-7. The guide rail is not present in the camera view.

Figure 3-7. A Screenshot of the Preliminary Experiment Video

Though no measurement is performed during this experiment, the objective of quickly verifying the hypothesis that a passive compliant tail driven by one single actuator can generate propulsion that is sufficient to propel the whole system forward is successfully attained. As shown in the video, the motor drives the tail through the crank-rocker mechanism and the tail oscillates around the axis within a range that is symmetric about the symmetric plane of the motor. More importantly, while the beginning of the tail is oscillated by the rocker, a clear undulatory motion is generated throughout the tail, which propels the whole unit forward along the guide rail with appreciable speed that is seemingly proportional to the voltage input applied to the motor. The response of the system is quick: when the power supply is turned on, the tail starts oscillating; when the voltage input gets higher, the frequency of tail oscillation increases at the same time, which results in a higher forward speed. It can be concluded that the hypothesis is correct and more rigorous experiments and analyses are worth to be carried out to further investigate how to improve the performance of the propulsion system. In particular, it needs to be investigated whether or not adjusting the stiffness of the passive compliant tail would improve the system performance to yield a fast swimming mechanism with high energy efficiency.

CHAPTER 4

SECOND ITERATION OF EXPERIMENTS

Based on the promising results from the preliminary experiment, an improved version of experiment is designed to gather useful data for further analysis and investigate the effects of some selected parameters on the performance of the system.

4.1 EXPERIMENTAL SETUP

In this iteration, the motor is kept the same to avoid major modifications in the design. Ideally a smaller motor can be used to reduce the total weight of the moving unit so that it may be easier to incorporate into the robot design in the future. But to save time and take advantage of the large quantity of such motors available in the lab, the same type of motor is used as the sole actuator to drive the tail. In addition, the material that is used to mold the tails also stays the same. The tails tested in this iteration have different dimensions, which are the main focus of the study at this stage. It would take much more time to test a variety of materials. The projected lengths of the crank, coupler and rocker in a 2D sketch similar to Figure 3-5 are not altered either.

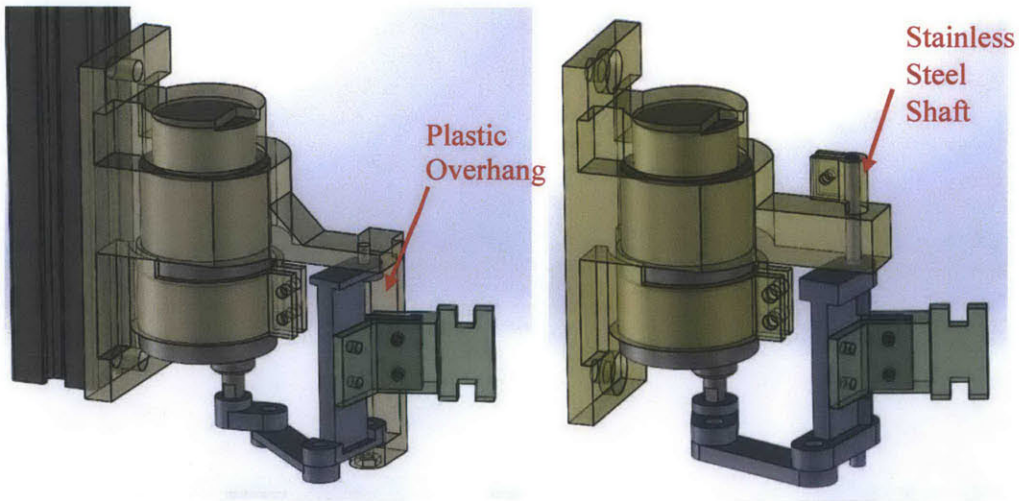

(a) Preliminary Design (b) Second Iteration

Figure 4-1. Comparison between the Preliminary Design and the Second Iteration

The motor housing and the crank-rocker mechanism are slightly modified to enhance the stability of the system. The CAD model of the improved version is illustrated in Figure 4-1, along with the comparison with the preliminary design. The most important difference is that in the improved design the rocker is connected with the motor housing through a steel shaft that has significantly higher Young's modulus than ABS plastic, which is the common material used by 3D printers. The rocker rotates freely around this shaft, which is tight fit into the motor housing and further secured with screws. In the preliminary design, the rocker is connected to the motor housing with an integrated overhang that is also 3D printed with ABS plastic. The superior Young's modulus of steel enhances the bending rigidity and thus reduces the undesired movement of the axis around which the rocker rotates.

Some additional improvements in the second iteration include: (1) the crank, coupler and rocker are thicker than before, (2) the screws that connect the crank, coupler and rocker are changed to M4 Friction-Resistant Brass Shoulder Screws (McMaster-Carr® Part No. 98451A117), instead of M2.5 zinc-plated steel screws used in the preliminary design, and (3) the nuts are replaced with M4 316 Stainless Steel Nylon-Insert Hex Locknut (McMaster-Carr® Part No. 94205A230). The increased thickness of the components reduces undesired deformation while the motor speed is high, though the components never experienced serious trouble during the preliminary experiment. A shoulder screw has a smooth surface that is not threaded. The components are specifically designed to take advantage of the shoulder area so that they can rotate around the smooth surfaces, which reduce friction during rotation. The locknuts can effectively prevent the screws from loosening during the experiment. Brass and 316 stainless steel are more resistant to water corrosion, so the screws and nuts are less likely to rust, which maintains the smoothness of the interface between the plastic components and screws. Figure 4-2 demonstrates the prototype based on the second iteration, and the carriage is also included in the figure. The total weight of the unit is 898.9 g.

The change in the experimental setup is that the guide rail is replaced by a 4 m long one that is available in the lab. The type of carriage and guide rail is Speed Demon OSG-25 purchased from LM76 [15]. The main reason to use such a long guide rail is to measure how long it takes for the system to reach steady speed after the motor starts rotating while keeping the voltage input constant. The long distance allows adequate time for the system to reach steady state.

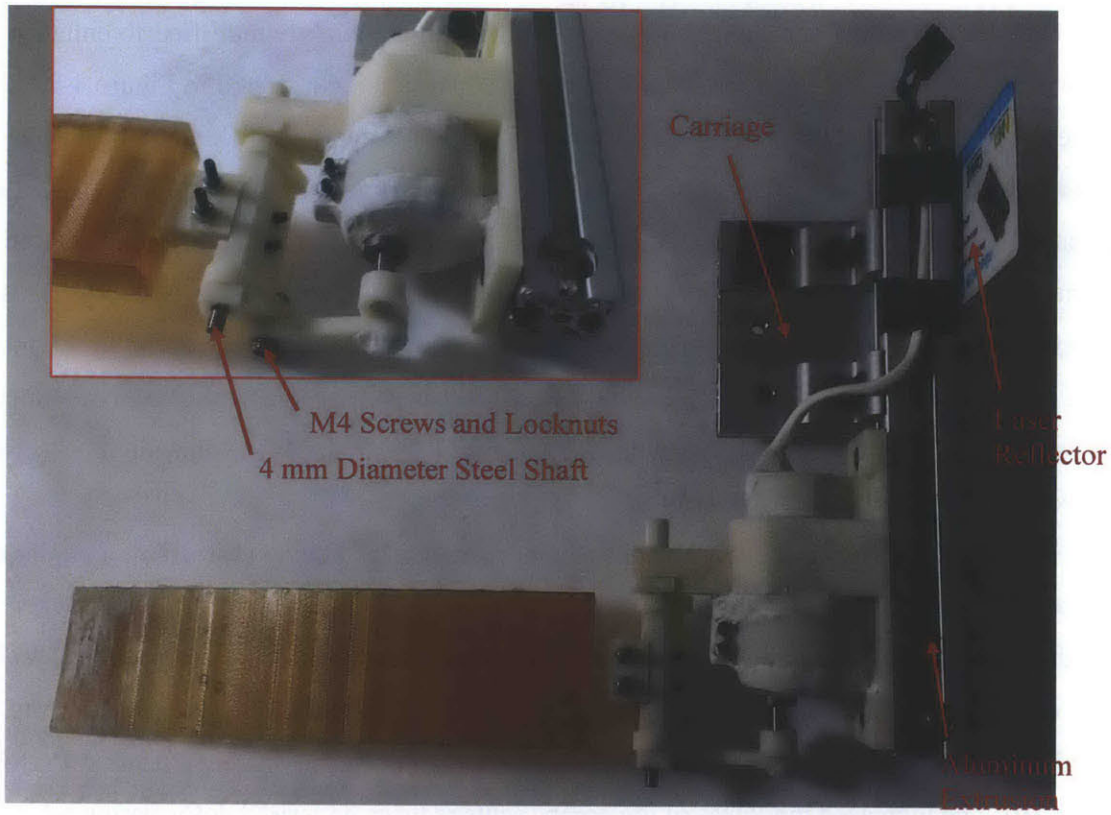

Figure 4-2. Prototype based on the Second Iteration of Design

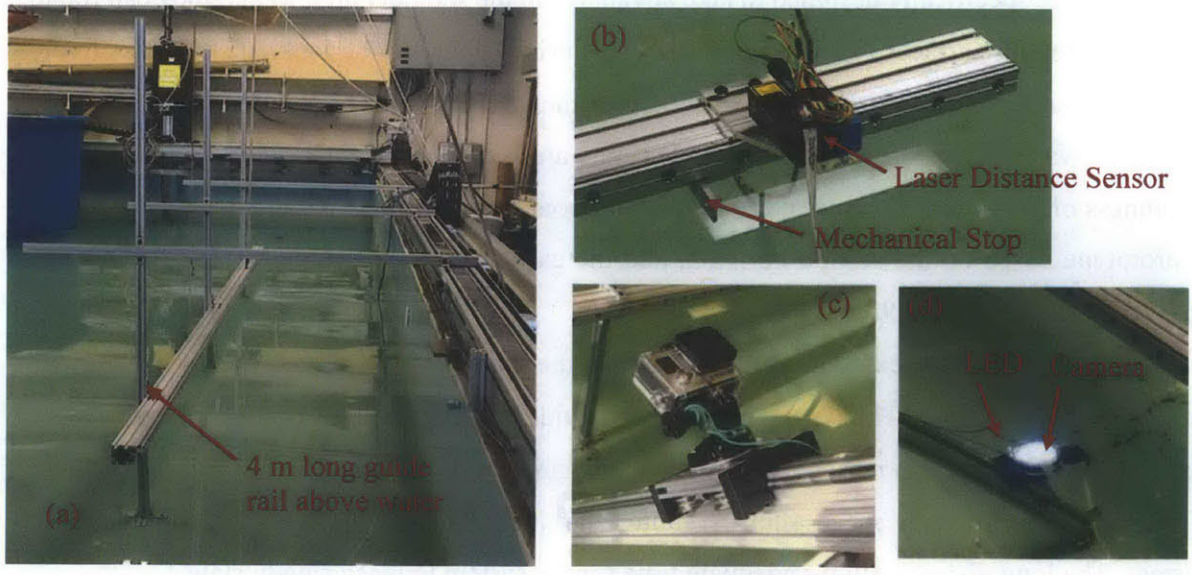

Figure 4-3. Guide Rail (a), Laser Sensor (b) and Camera (c, d) Setup

It is challenging to set up such a long guide rail in an environment with water. Thanks to Prof. Franz Hover, the entire experimental setup could be installed in the giant testing pool in MIT 1-225 (Building 1 Room 225). The entire guide rail is supported by three aluminum extrusions vertically, and it is suspended right above water to avoid total submergence and potential corrosion. The guide rail is not easy to be disassembled from the supporting structure for frequent maintenance. The carriage, connected with the motor and tail through a short aluminum extrusion, is put on and taken away from the guide rail before and after each experiment. The distance between the guide rail and water surface is adjusted carefully so that the tail can be entirely submerged under water. Figure 4-3 (a) demonstrates the setup of the guide rail.

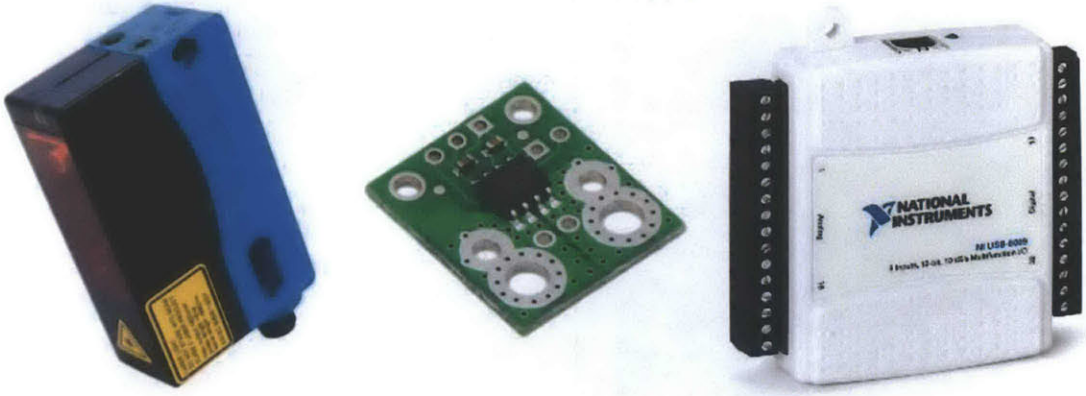

(a) Laser Distance Sensor (b) Current Sensor (c) Multifunction DAQ

Figure 4-4. Sensors and DAQ

To measure the speed of the unit that is propelled by the oscillating tail, a Micro-Epsilon optoNCDT ILR 1030 Laser Distance Sensor, shown in Figure 4-4 (a), is installed at the end of the guide rail [16]. The measuring range of this type of sensor is between 2 m and 50 m, and more importantly, the response time is merely 10 ms. The short response time is critical because the distance that needs to be measured is constantly changing while the unit is moving along the guide rail. If the response time were too long, the distance measurement would not be accurate for further analysis to obtain speed measurement. A plastic card with reflecting tape on the side facing the laser sensor is attached to the aluminum extrusion that connects the carriage and motor housing. This card is intended to reflect the laser more effectively so that the laser sensor can measure the changing distance continuously. A mechanical stop is installed right in front of the laser sensor to

avoid collision and prevent the moving unit from falling from the guide rail when it reaches the end.

To measure the power input into the system, an ACS714 Current Sensor Carrier from Polulu, shown in Figure 4-4 (b), is installed along the wire that connects the power supply and the motor [17]. This current sensor measures +/- 5 A current with a typical error of +/- 1.5%. The voltage remains constant throughout each individual experiment, so the power input can be calculated by multiplying the measured current and the set voltage. It is essential to measure the power input in order to compute the cost of transport when analyzing the system performance.

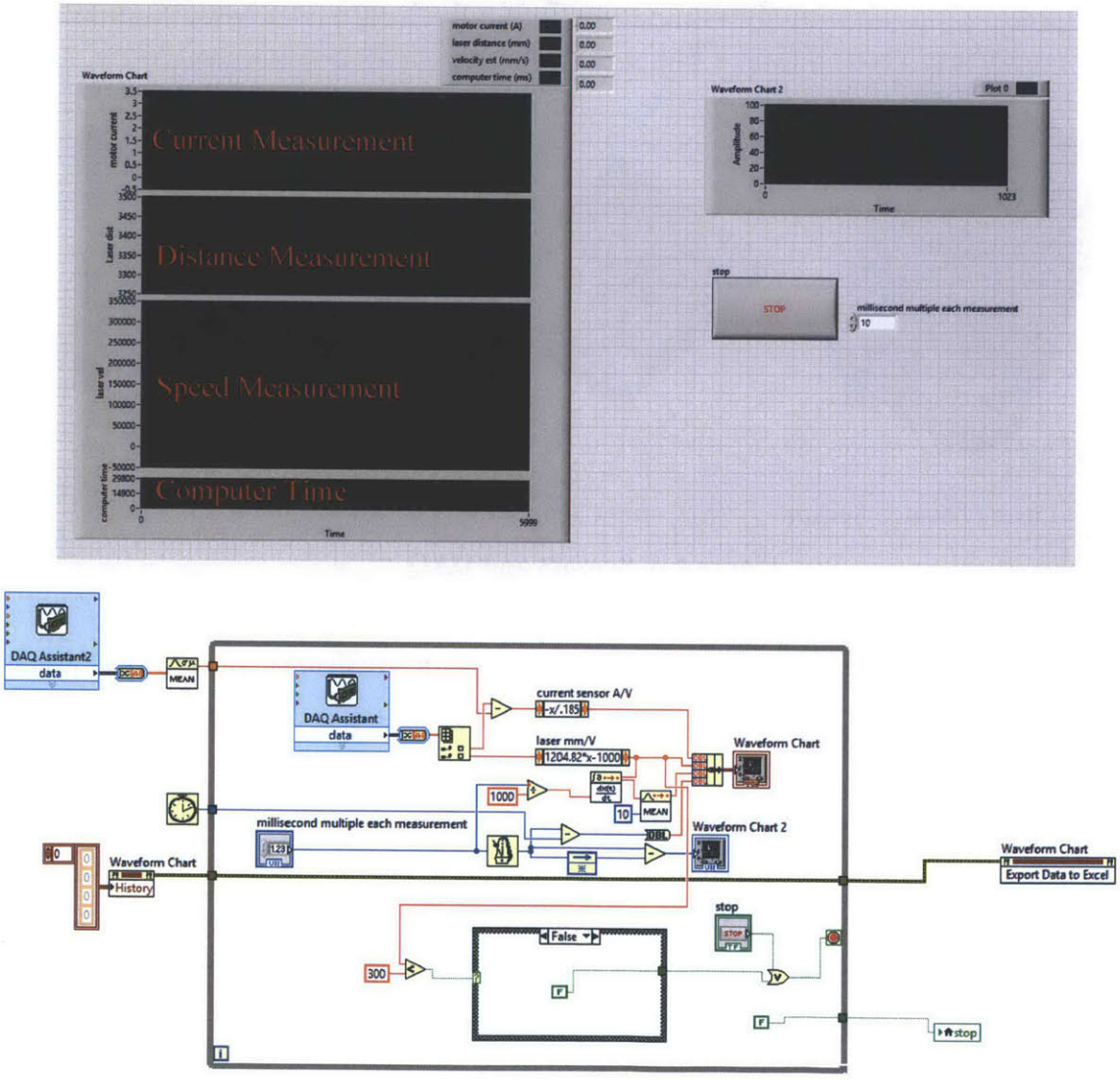

Figure 4-5. LabVIEW Program for Data Acquisition

To record the distance measurement from the laser sensor and the current measurement from the current sensor simultaneously, it is necessary to set up a data acquisition system that displays the data in real time for quick verification and records the data in an organized and convenient way. A National Instruments® USB-6009 Multifunction DAQ, shown in Figure 4-4 (c), is adopted to convert the analog inputs from the current and laser sensors into digital signals and transfer the data into a laptop that runs a customized LabVIEW program, which displays the data in real time and exports them into Excel spreadsheets. The DAQ has an analog-to-digital-conversion resolution of 14 bit and the maximum sampling rate of 48 thousand samples per second, which are more than enough for this application. Figure 4-5 demonstrates the LabVIEW program that was built with the help from Albert Wang, a Ph.D. candidate in the MIT Biomimetic Robotics Lab. The current and distance measurements are directly acquired from the DAQ. The speed measurement is the instantaneous differential of the distance measurement. It is mainly recorded for verification purpose during data analysis, but in fact the speed data are not used for analysis.

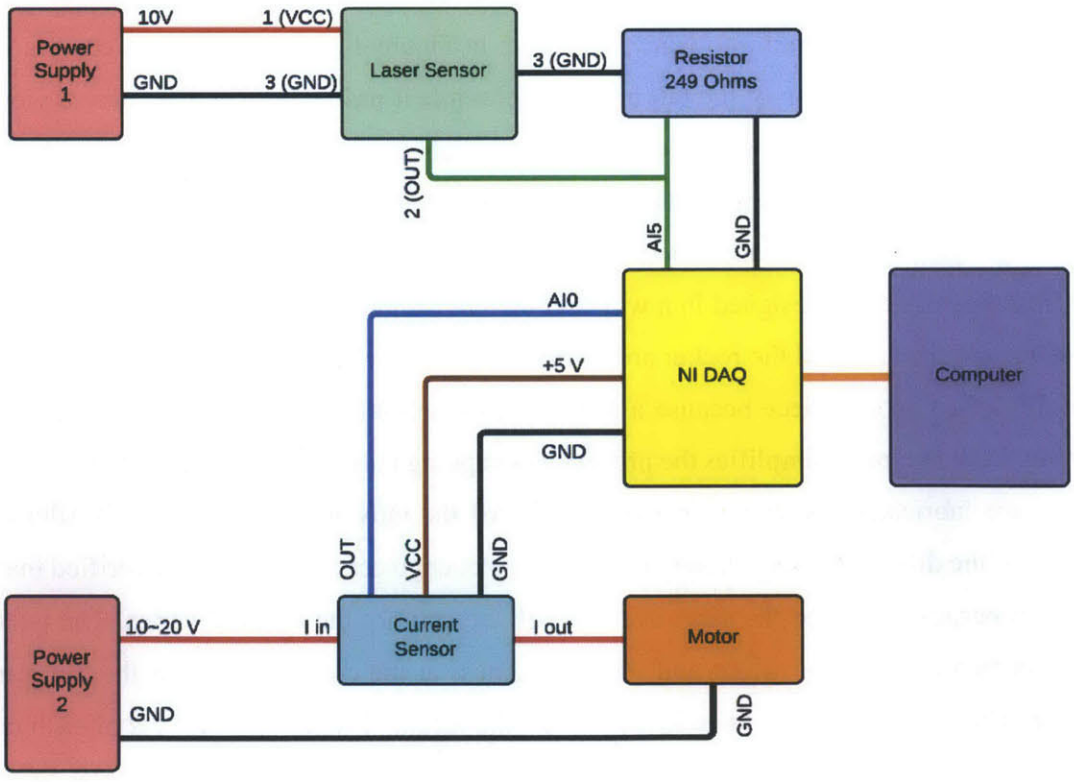

Figure 4-6. Overall Experimental Setup

A resistor needs to be connected between the ground and output pins of the laser sensor. The resistance value must be calculated carefully. According to the manual of the laser sensor, the default setting of the analog output is 4 mA corresponding to 200 mm, and 20 mA corresponding to 5000 mm. Since the total length of the guide rail is 4 m, it is not necessary to adjust the setting. The analog input pins on the DAQ can take up to 10 V, but the resistor value is calculated for Arduino Uno, whose analog input pins can only accept voltage input up to 5 V. To map the $4-20$ mA current output from the laser sensor into the $0-5$ V voltage input that is acceptable to Arduino Uno, a 249-Ohm resistor is placed between the ground and output pin of the laser sensor. A 499-Ohm resistor can be used instead to fit better with the DAQ. But since the resistor is soldered onto the laser sensor already, it is not changed for this experiment.

To capture the motion of the tail while it is propelling the moving unit forward along the guide rail, a GoPro® Hero3+ Black Edition camera is used to record videos during experiments [18]. The GoPro® camera has a few advantages: (1) it comes with a waterproof housing, (2) it is able to shoot videos at a high frame rate (up to 240 frames per second under WVGA mode), and (3) it is inexpensive, versatile and shoots high quality videos. The camera is installed on a carriage which slides along a guide rail into water, as shown in Figure 4-3 (c) and (d). The camera faces upward to capture the motion of the tail under water while it passes through the camera view. If the camera were placed above water, the reflection of light by the water surface might block the camera view and the camera would not be able to capture the tail motion clearly. An LED light is also installed right next to the camera to provide more lighting while the videos are taken.

The mechanism is designed in a way that the tail can be easily assemble and disassemble from the rocker. The tail and the rocker are connected with four M2.5 screws. The tail and rocker are not fabricated as one piece because a series of different tails are expected to be tested, and separating those two parts simplifies the process of swapping tails. In this iteration of experiments, four tails are fabricated, as shown in Figure 4-7. All the tails are molded with Vytaflex® 20 regardless of the different colors shown in the figure. An engineer at Smooth-on® verified that the material properties should be the same even though the color of the material varies. The tails are different in two dimensions: width and initial thickness at the conjunction with the 3D printed connector. The thickness varies linearly along with the length. The initial thickness of each tail is indicated in Figure 4-7. The width stays constant along the length. All four tails are 19-cm long,

constrained by the maximum size of the tail molds that can be fabricated on the 3D printer available in the lab. The name of each tail is listed on the left in Figure 4-7.

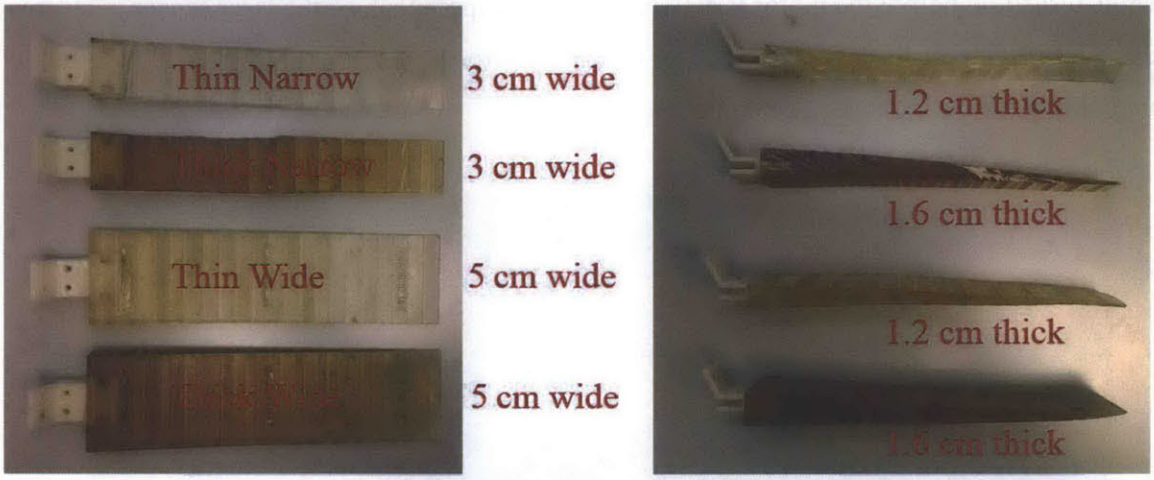

Figure 4-7. Four Types of Tails

4.2 RESULTS AND DISCUSSION

A series of experiments were conducted with three controlled variables: (1) width of the tail, (2) thickness of the tail, and (3) voltage applied to the motor. There is a large number variables that can be chosen to vary during experiments, for example, material of the tail, length of the tail, type of the motor, range of oscillation of the tail, just to name a few. It is infeasible to vary so many different properties in a limited number of experiments. Therefore the study focuses on the influence due to merely three variables on the system performance.

A video that was shot outside the testing pool is available on YouTube [19]. A screenshot of the video is shown in Figure 4-8. It demonstrates how the tail propels the whole unit forward along with the guide rail. Another video that was shot using the GoPro® camera under water is also available on YouTube [20]. This video demonstrates the undulatory motion of the tail under water while it is moving forward. It is noticed that the tail may be too close to the water surface such that while the system is operating, the tail generates appreciable but undesirable splashes which increase the drag that the system needs to overcome. Figure 4-9 presents the current vs. time and distance vs. time plots for the experiment on the Thick Narrow tail when the voltage input is 20 V. In the distance vs. time plot, the distance measurements are reversed. At the beginning of

each experiment, the measured distance should be the largest, while the moving unit is far away from the laser sensor. The measured distance should be decreasing while the moving unit is moving toward the laser sensor positioned at the end of the guide rail. The LabVIEW data acquisition system is turned on before the motor is activated in each experiment, so the laser sensor measures the constant distance and the current sensor measures zero current for a few seconds while the moving unit is stationary at the beginning.

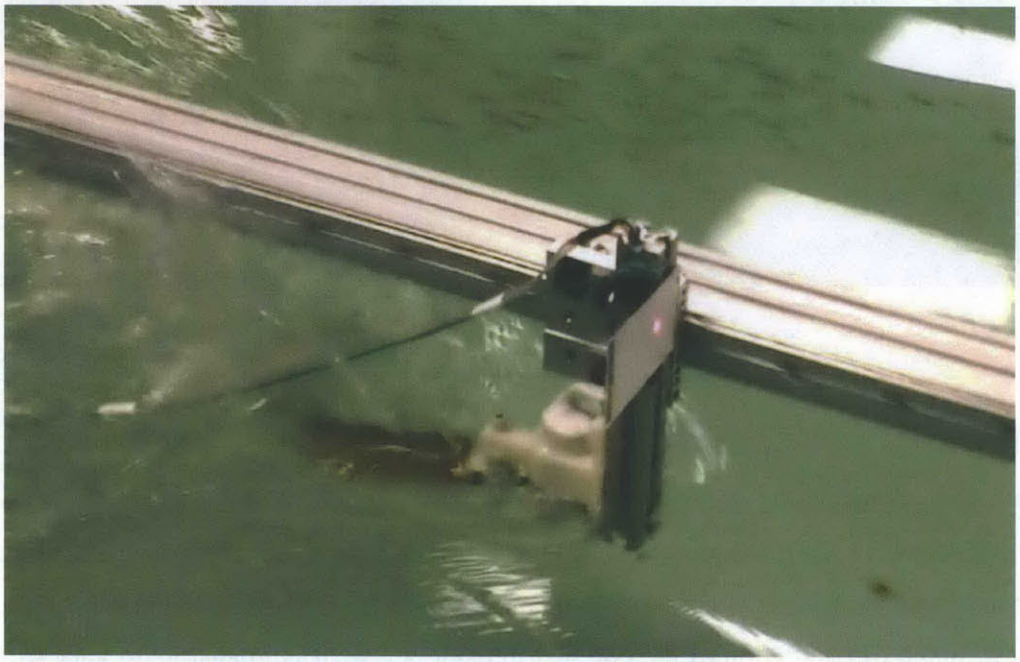

Figure 4-8. A Screenshot of the Experiment Video

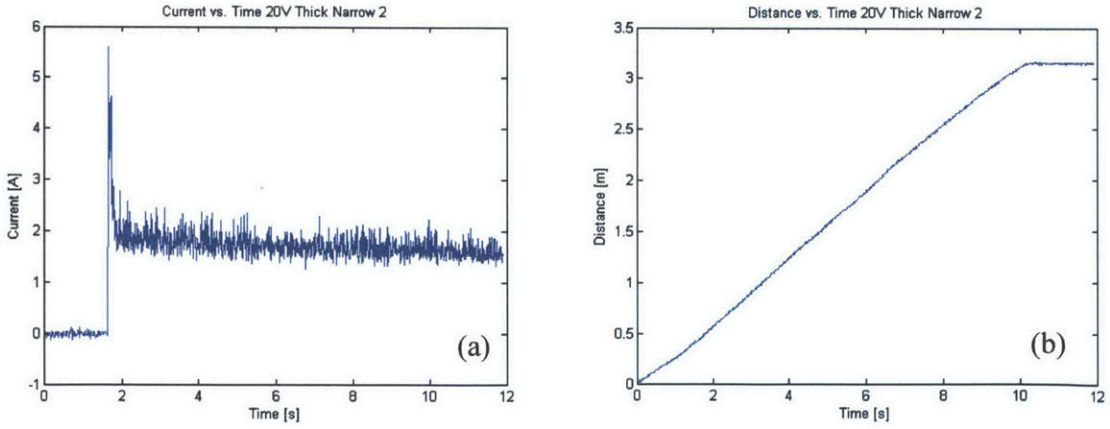

Figure 4-9. Current vs. Time (a) and Distance vs. Time (b) Plots

Each tail is tested at five different voltages (5 V, 10 V, 15 V, 20 V and 25 V), so there are 20 individual experiments in total. In the current vs. time plot, the current value is around zero before the power supply is turned on to apply a voltage on the motor. The current value shoots up when the power supply is switched on, and it oscillates roughly around a constant value while the moving unit is propelled forward by the tail along the guide rail. The current does not stay constant because the amount of reaction force exerted by the crank-rocker mechanism and the connected tail that the motor needs to overcome is varying during operation. Instead of using instantaneous values to represent current during each experiment, the average value of the instantaneous values after the transient phase is used. For example, the average value of current after 2 s in Figure 4-9 (a) is about 1.7 A. Eliminating the transient phase, the distance vs. time curve is close to a straight line with a constant slope. The average speed of the moving unit in each experiment can be estimated as the slope of this straight line. For example, in Figure 4-9 (b), the slope of the straight line before 10 s is about 0.33 m/s, which is regarded as the average speed of the moving unit. A MATLAB script, presented in Appendix E, is written to process the current and distance data for all 20 experiments together and generate summary plots to compare the experiments.

Figure 4-10 illustrates the average speed vs. average current plot and Figure 4-11 illustrates the cost of transport vs. voltage for all 20 experiments. There are four curves with distinct colors, each representing a type of tail. Table 4-1 summarizes the data based on the different types of tails.

As shown in Figure 4-10, a general trend is that for each tail, as the voltage input increases, the average current and the average speed both increase with diminishing margin. The average speed starts to saturate after the voltage input exceeds 15 V, even though the current drawn keeps increasing. Overall the Thin Wide tail, shown in pink, seems to have the best performance among all four tails, as its average speed at each different voltage level is better than that of any other three tails. The Thin Wide tail also achieves the highest speed, which is 0.43 m/s when the voltage input is 25 V. The Thick Wide, Thick Narrow and Thin Narrow are ranked the second, third and fourth places, respectively, according to the average speed at each voltage level. The order is consistent with respect to voltage, as shown more clearly according to the data summarized in Table 4-1.

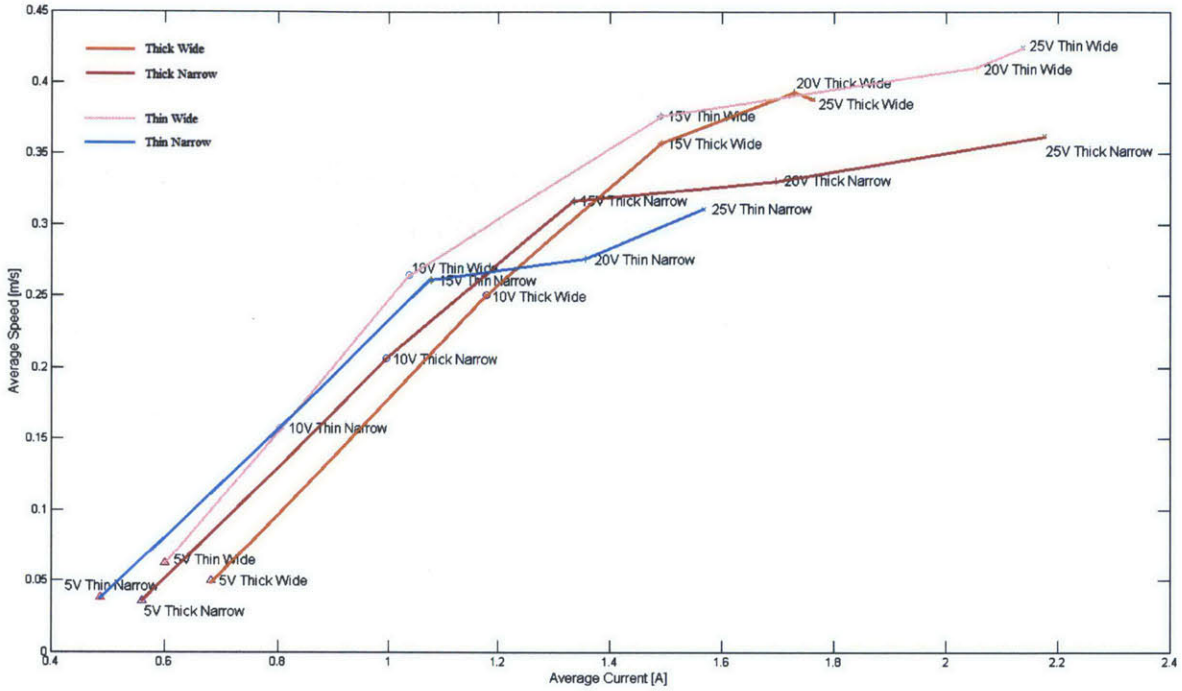

Figure 4-10. Plot of Average Current vs. Average Speed

It is not fair to compare the performance of the system with different tails based on the average speed only, because apparently the current drawn during each experiment varies as well. Therefore the cost of transport is brought in as a critical criterion to evaluate the system performance. The cost of transport quantifies the energy efficiency transporting an animal or vehicle from one place to another. It is defined according to Eq. (4-1) below:

$$COT = \frac{P}{mgv}, \tag{4-1}$$

where COT represents the cost of transport, P is the power input to the system, m is the mass of the system, g is the gravitational acceleration, and v is the constant velocity of the system [21]. The power input to the system is calculated as the product of the average current and set voltage for each experiment.

Table 4-1. Summary of Data for Different Tail Types

Thick Narrow	Voltage [V]	5	10	15	20	25
	Current [A]	0.56	0.99	1.34	1.70	2.18
	Speed [m/s]	0.04	0.21	0.32	0.33	0.36
	CoT	8.97	5.55	7.28	11.79	17.28
Thick Wide	Voltage [V]	5	10	15	20	25
	Current [A]	0.68	1.18	1.49	1.73	1.76
	Speed [m/s]	0.05	0.25	0.36	0.39	0.39
	CoT	7.86	5.40	7.20	10.12	13.04
Thin Narrow	Voltage [V]	5	10	15	20	25
	Current [A]	0.49	0.80	1.08	1.36	1.57
	Speed [m/s]	0.04	0.16	0.26	0.28	0.31
	CoT	7.35	5.86	7.11	11.31	14.50
Thin Wide	Voltage [V]	5	10	15	20	25
	Current [A]	0.60	1.04	1.49	2.05	2.14
	Speed [m/s]	0.06	0.26	0.38	0.41	0.43
	CoT	5.53	4.51	6.83	11.53	14.48

According to Figure 4-11, overall the lowest cost of transport occurs at 10 V when experimenting on the Thin Wide tail, which is 4.51. The Thin Wide tail also has the lowest cost of transport at 5 V, 10 V and 15 V, compared with the other tails. On the contrary, the Thick Narrow tail has the highest cost of transport at all voltages except at 10 V, where the Thin Narrow tail tops the other tails. Evaluating the data of cost of transport leads to a preliminary conclusion that tails with larger side area and smaller cross-sectional area tend to have lower cost of transport.

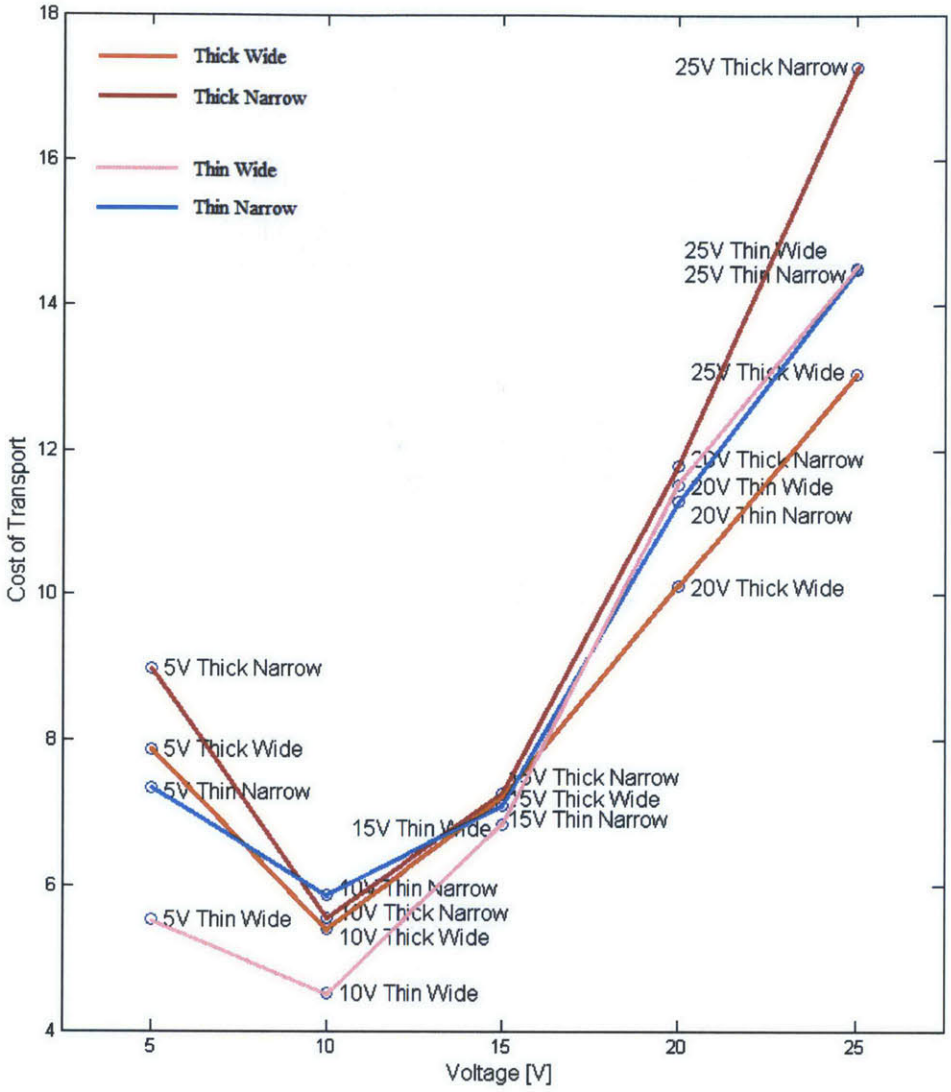

Figure 4-11. Cost of Transport vs. Voltage

The larger side area means the tail can push more water around while oscillating and thus can generate higher propulsion if the frequency is roughly the same when compared to those with smaller side area. If a small segment of the tail, viewed from the top, is considered for analysis for example, the same driving frequency of the tail is equivalent to the same change in linear velocity relative to surrounding water. A tail with larger side area would have more segments like this that can accelerate more water simultaneously and thus the change in linear momentum would be larger than that produced by a tail with smaller side area. The angular speed of the motor is inevitably

different when driving different tails, but the variance is assumed to be small. It is worth to measure the motor speed for verification.

Figure 4-12. A Rigid Plastic Tail with the Same Dimensions as the Thin Wide Tail

The smaller cross-sectional area of the tail enhances its flexibility. A thick tail is more difficult to bend compared to a thin one. However, it is not desirable to make the tail too thick or too thin. An extreme case would be a completely rigid tail, which can push water around more firmly. In order to test the hypothesis that a flexible tail is better than a rigid tail in terms of generating propulsion, a plastic tail, shown in Figure 4-12, is fabricated on the 3D printer with the same dimension as the Thin Wide tail. When the motor is driving this rigid tail, it can barely propel the whole unit forward. Instead, the carriage moves back and forth on the guide rail regardless of the voltage input to the motor. Therefore, it is proven that a flexible tail is indeed more advantageous than a rigid tail in terms of generating propulsion. Though an extremely flexible tail is not fabricated, it can be conjectured that such a tail would not work well either because it could barely maintain its side area while being driven by the motor. In conclusion, there should be an optimal thickness at which the tail can operate with the lowest cost of transport while keeping all the other variables the same. If the thickness is variable along the length, it is equivalent to finding an optimized stiffness profile, which is the ultimate goal of this research project. More experiments need to be conducted in order to achieve more detailed conclusions.

4.3 PROBLEMS AND IMPROVEMENTS

The lowest cost of transport is 4.51, whereas the highest cost of transport is 17.28. The values are appreciably higher than those of underwater animals. The values of cost of transport of real

swimmers are between 0.41 and 0.81, roughly an order of magnitude lower than the experimental results [22]. The real underwater animals, especially fish, have been highly optimized throughout their evolution in time. It is admittedly difficult to create a man-made system that can achieve similarly high energy efficiency as real swimmers. A propulsion system with a passive tail driven by a single actuator may never be more efficient than real fish. However, there are several other aspects that can be modified in order to bring the cost of transport more close to that of real swimmers. First of all, though the tail and motor are entirely submerged under water, they are very close to the water surface such that when the tail propels the moving unit forward, it results in undesired splashes, shown in Figure 4-8, that may lower the energy efficiency significantly. Turbulence at the surface of the water increases drag, and the transfer of momentum to water is more efficient when swimming well below the water surface and more forward thrust is created as a result [23]. Secondly, it is noticed that the whole unit vibrates considerably when moving along the guide rail, and the magnitude of vibration increases when the voltage input to motor increases. The undesired vibration also contributes to the relatively high cost of transport and thus should be reduced if possible. The carriage is not designed to operate sideways along the guide rail and not good at overcoming vibrations perpendicular to the mounting surface. A different type of carriage may be used to remedy this issue. Last but not least, the whole unit is not designed to be streamlined. The current configuration has a flat surface in the front and the four bar linkage are in direct contact with water. A streamlined case that enclose the four bar linkage may help reduce the drag.

To compare the experimental results with the simulation, it is necessary to capture the tail motion accurately. Since the tail is moving very close to the water surface, the resulted splashes are inevitably displayed in the background which make it difficult to identify the tail shape in each frame. The splashes need to be reduced in future experiments.

The aforementioned problems are addressed in the next iteration of experiments.

CHAPTER 5

THIRD ITERATION OF EXPERIMENTS

Though the results from the second iteration of experiments are promising and provide some valuable guidelines for future experiments, several aspects of the experiments need to be improved as discussed in Section 4.3. Unfortunately, the intended improvements discussed in this chapter do not work well in real experiments, so another iteration is discussed in the next chapter. Nevertheless, the lessons learned from these failures are valuable for the design of the experiments.

5.1 REDUCING SPLASHES AND VIBRATIONS

The splashes mainly cause two problems in the second iteration of experiments. First of all, the splashes result in a higher cost of transport because more energy is spent on generating the undesired waves and splashes and overcoming the increased drag consequently. Secondly, when the camera is placed under water facing upward to capture the motion of the tail, the appreciable splashes and waves must interfere with the tail motion in the video, which makes it difficult to identify the exact shape of the tail at each time step. Therefore, the imminent problem at hand is how to reduce the splashes and waves at the water surface.

To minimize the splashes and waves generated along the water surface, the motor and tail should be submerged well below the water surface. One intuitive solution is to extend the aluminum extrusion, shown in Figure 4-2, which connects the carriage and the motor housing. The distance between the carriage and the water surface is virtually fixed, because the carriage is moving along the guide rail that is set at a fixed level above the water surface. Without changing the guide rail and the supporting structure, a quick way to lower the positions of motor and tail is to extend the aluminum extrusion, which decides the distance between the water surface and the tail. Theoretically it should work well, but in reality such a simple modification results in other problems. The extended aluminum extrusion allows a longer moment arm between the motor and the carriage. While the motor is spinning, it causes undesired vibrations of the carriage along the guide rail, a phenomenon observed in the second iteration of experiments. The undesired vibrations are enhanced by the extended moment arm, and when the voltage input is relatively low, for

example, at 5 V, the tail can barely propel the whole unit forward along the guide rail because the vibrations severely impede the forward motion. When the voltage input to the motor is higher, the tail can propel the whole unit forward, but the vibrations are more significant compared to those observed in the second iteration of the experiments. Though no measurements are taken during the trials, it is reasonable to conclude that the cost of transport is higher than before.

Another less quick but still manageable solution is to lower the guide rail below the water surface. In that case, not only would the motor and tail be submerged under water, the carriage would be as well. More components under water might increase the drag, but since the splashes and waves along the water surface could be reduced, the overall drag might be lower than before. Lowering the entire guide rail, which is 4-m long, is a time-consuming process, but the modification can be finished in one day. The most severe problem associated with this solution, which ultimately caused a denial, is that the guide rail rusts quickly when submerged under water. Figure 5-1 illustrates the rust developed along the guide rail, especially the rods that are in direct contact with the wheels on the carriage, after it was submerged under water for about two days. Since it is difficult to take the guide rail out of water after each experiment, it is almost impossible to keep it dry while not conducting experiments.

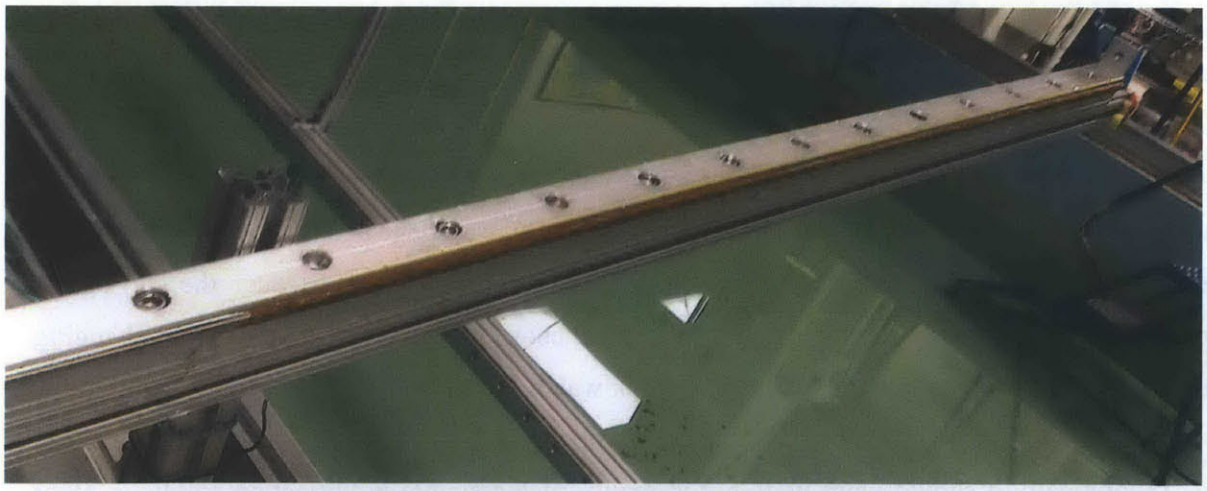

Figure 5-1. Rust Developed along the Guide Rail

According to Figure 4-9 (a), the transient phase is merely 0.2 s, after which the whole moving unit achieves steady state. Though the linear speed still fluctuates while the tail is oscillated

by the motor and four bar linkage, the average linear speed is fairly constant, as shown in Figure 4-9 (b). Therefore it is not necessary to use such a long guide rail to reach the steady state.

Since the original guide rail cannot satisfy the requirements and it is not necessary to maintain the length, a new guide rail and carriage system is designed with the hope to reduce the splashes and waves along the water surface as well as the vibrations of carriage caused by the motor. As discussed before, the motor and tail should be submerged well below the water surface to reduce the splashes and waves along the water surface, and the distance between the carriage and motor should be shortened to reduce the vibrations. The guide rail needs to be submerged under water, if necessary, to satisfy these two requirements at the same time. Thus the materials used to build the guide rail should be stainless steel and anodized aluminum that are not easily corroded in water. The carriage, on the other hand, does not have to be highly resistant to corrosion because it does not stay on the guide rail permanently. After each experiment it is taken off from the guide rail along with the motor and tail. However, it would be ideal to have a carriage that is easy to dry to avoid rust.

The Track Roller Carriage for T-Slotted Framing (McMaster® Part No. 9904K1) is selected for the new experimental setup. The main reason for using this type of carriage is because it does not require any special guide rail. The Extrusions for Aluminum T-Slotted Framing that is widely adopted for prototyping purposes can be used as the guide rail for the tracker roller carriage. The aluminum extrusions are anodized so they are unlikely to be corroded in water. The wheels of the tracker roller carriage are made of plastic. Figure 5-2 illustrates the experimental setup. To minimize the undesired vibrations during experiments, two aluminum extrusions are used to constrain a pair of track roller carriages, which are connected with a piece of transparent plastic fabricated on a laser cutter. The wheels are inserted into the T-slots on the aluminum extrusions. Such a system can reduce undesired motions in pitch, roll and yaw directions. The motor and tail unit is still connected to the carriage by an aluminum extrusion. The red line in Figure 5-2 shows the water level. The motor and tail are about 8 cm deeper into water than in the second iteration of experiments. Only one of the carriages is submerged under water, whereas the other one is above water. The fewer components of the moving unit under water can help limit the drag. The carriages can move along the aluminum extrusions freely when driven by hand. The distance between the two aluminum extrusions is adjusted to find a balance point between friction and rolling reductions.

There is less friction if the two aluminum extrusions are further apart, but meanwhile the rolling motion cannot be constrained well.

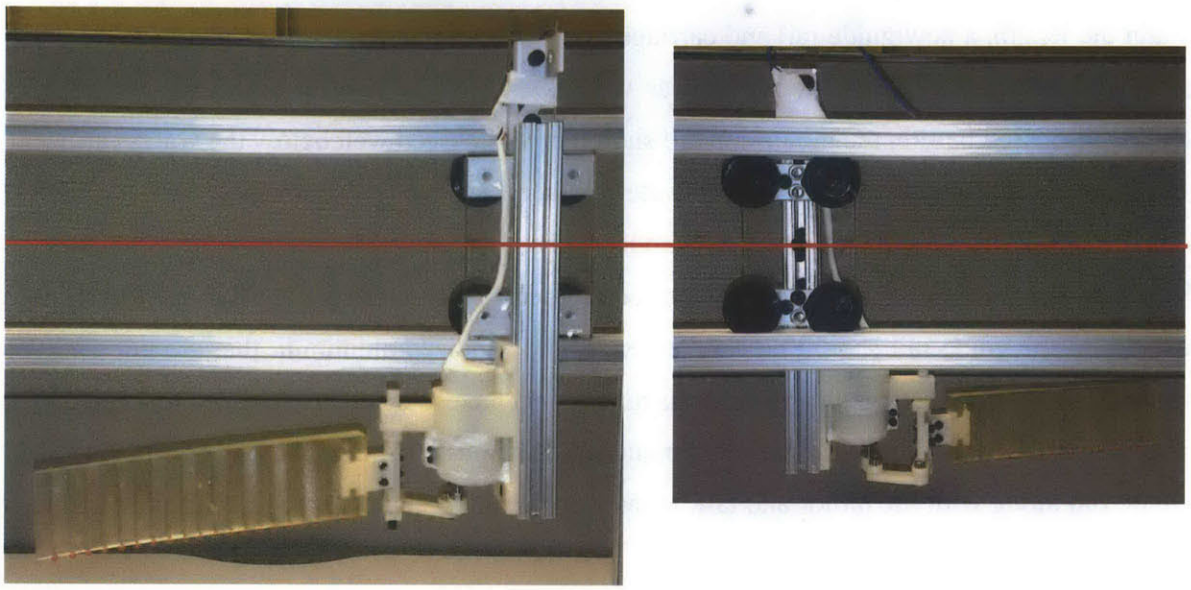

Figure 5-2. Third Iteration of Experimental Setup

This experimental setup is easy to construct. The only component that needs to be fabricated is the plastic piece that connects the carriages and motor housing. Using the laser cutter the fabrication takes less than half an hour in total. In addition, the carriages and aluminum extrusions are less expensive than the components used in the previous experiments, though the friction between the wheels and guide rails is more appreciable. However, since the moving unit is well constrained by the two aluminum extrusions, it is reasonable to expect that undesired motions can be reduced significantly.

Unfortunately this experimental setup does not work well as intended. When experimenting in water, no matter what the voltage input to the motor is, the tail cannot propel the moving unit forward. It is stuck at the initial position, and as a result the entire structure, including the aluminum extrusions, are vibrating. The vibrations are so significant that the aluminum extrusions are forced to move up and down noticeably. This negative phenomenon was not observed in the second iteration of experiments in which the guide rail, mainly made of steel, is secured onto a wider and stronger aluminum extrusion. It is suspected that the distance between the two aluminum extrusions is so small that the carriages were impeded to move forward due to

vibrations and increased friction between the plastic wheels and aluminum extrusions when submerged under water. However, even after increasing the distance between the two aluminum extrusions, the moving unit still vibrates at the initial position without moving forward. It is not clear why this experimental setup failed. It is necessary to come up with a different design to satisfy the requirements mentioned at the beginning of this section.

5.2 ADDITIONAL DEGREE OF FREEDOM ON THE TAIL

Besides the tail is too close to the water surface, another reason that the tail generates splashes and waves may be that the beginning of the tail is too rigid. The tail connector, a 3D printed rigid component, is overmolded into the tail, as shown in Figure 3-6. The tail connector is also shown in Figure 3-3 in the CAD model. Since the tail connector is completely rigid and directly connected to the rocker, the undulatory motion propagates through the tail from this component. The tail is supposed to be passive, which indicates that when it moves in water, the hydrodynamic forces are an important factor to affect its motion. The rigid tail connector that is directly attached to the rocker is not affected by the hydrodynamic forces that much compared to the rest of the tail that is made of Vytaflex® 20, which is flexible polyurethane. Though it is an effective way to transmit the undulatory motion commanded by the motor and four bar linkage through this rigid tail connector, the fact that the rigid component does not interact with the surrounding water as gently as the flexible polyurethane raises the concern that it may generate excessive turbulence while moving in water which results in additional drag. Therefore, an additional degree of freedom between the rocker and tail may help improve the flexibility at the beginning of the tail and help reduce turbulence and drag consequently.

Figure 5-3 compares the original design with the revised design. In the original design, the rigid tail connector is attached to the rocker with four screws. The tail connector, which is molded into the flexible tail, oscillates directly along with the rocker. In the revised design, the tail connector is no longer needed. A stainless steel shaft, which is molded into the tail, is inserted into the holes on the new rocker. To simplify the assembling process, the rocker is divided into four pieces, shown as Part 1-4 in Figure 5-3. The tail is mounted onto the rocker, Part 1 and 2, through the stainless steel shaft. Part 1 and 2 of the rocker are connected by two pieces of plastic, secured by two pairs of screws and nuts together. The shaft molded into the tail rotates freely in the mounting holes on the rocker. The rocker rotates around the other stainless steel shaft that is tight

fit into the motor housing, which is the same as in the original design. The configuration of the four bar linkage remains unaltered.

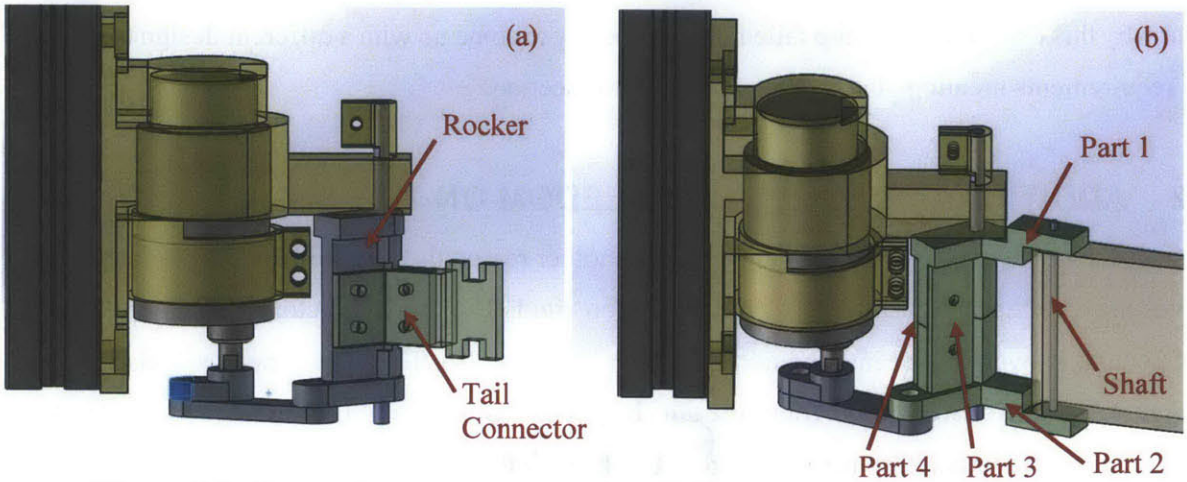

Figure 5-3. Comparison between Original Design (a) and Revised Design (b)

After all the newly designed components are assembled, the revised tail with the additional degree of freedom is tested on the experimental setup shown in Figure 4-3 before it was disassembled and replaced by the setup in Figure 5-2. Unfortunately, after the motor is turned on, the tail moves back and forth along the same straight line and cannot generate the undulatory motion like the original design. An experiment video is available on YouTube [24]. It is suspected that the initial position of the tail might affect its performance, but centering the tail before it is actuated did not change the situation. Once the tail is aligned to the straight line along which it encountered the least resistance from water, it stays along the line to move back and forth without propelling the moving unit forward. Not only does adding an extra degree of freedom at the beginning of the tail not help improve the system performance, it actually ruins the capability of the tail which should be able to generate propulsion. Therefore, the revised design is abandoned and the original design is kept for later experiments.

5.3 CAPTURING DETAILED TAIL MOTION

As discussed in Section 4.3, it is necessary to capture the detailed motion of the tail during experiments to compare the experimental and simulated results. Ideally the exact shape of the entire tail should be recorded continuously with a camera during an experiment, and the view

should not be distorted by splashes and waves resulted from the tail motion. In reality, it is considerably challenging to record the shape of the entire tail, which would be a continuous curve. In addition, no video is actually continuous; every video has a certain frame rate, which is usually 30 frames per second. However, 30 frames per second may not be fast enough to record the tail motion accurately, especially when the voltage input to the motor is high, which corresponds to high frequency of tail oscillation. One of the reasons that GoPro® Hero3+ Black Edition is selected to record a video during each experiment is that it can record at 240 frames per second under the WVGA mode. The resolution does not have to be very high as long as it is easy to identify the tail shape in each frame. If the frame rate were too low, the tail shape in each frame might be blurred, which would make it difficult to describe the shape with a curve.

To identify the curve that can describe the tail shape in each frame, it is intuitive to choose a number of characteristic points, or markers, along the tail. If the markers have distinct color that is convenient to identify against any other objects in the video, a computer program may be able to capture the markers in each frame. Indeed, there is an open source program named Tracker with such capability [25]. A user can load a video in the Tracker program and set up an appropriate coordinate system and scale based on which the position of each marker is identified. The user can choose to track any point with distinct color compared to the surroundings. The more distinct the color is, the easier it is for the program to track the marker accurately. Once a marker is clearly defined in a frame, the program is supposed to identify it in the subsequent frames automatically. This is particularly useful when the frame rate is high. If the frame rate of the video is not high enough, a marker on the tail may move a significant distance away from the position in the previous frame, then it would be difficult for the program to track the marker accurately.

Since the tail has a uniform color, it is necessary to create physical markers along the tail, otherwise it would be troublesome to identify which points to track. A series of pins with plastic heads are chosen to be embedded into the tail. The plastic heads have various colors, and the red ones are chosen because nothing else in the experimental setup or the testing pool is in red. It should be easy to identify them in the video. The more markers that are tracked in an experiment video, the more accurately a curve can be identified to describe the tail shape in each frame. In total, 21 pins are embedded into the tail, about 5 mm apart from each other. Figure 5-4 demonstrates the pins on the tail. The plastic pins are very light in weight and the metal part that inserts into the tail is about 4 mm long on average. Inevitably embedding the pins affect the

flexibility of the tail, but its overall performance is not expected to be altered significantly by the pins.

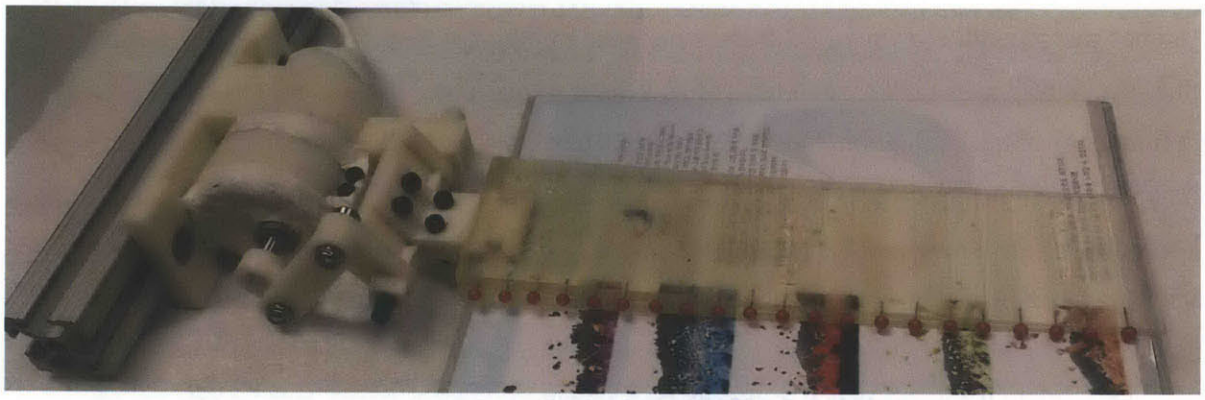

Figure 5-4. Embedded Plastic Pins on the Tail

The GoPro® camera is placed on the bottom of the testing pool, facing upward to capture the tail motion while it moves right above the camera. Both WVGA (240 frames per second) and 720P (120 frames per second) modes are tried. Unfortunately the tail motion is not captured under either mode. There are two primary reasons: (1) the frame rate is not high enough; and (2) the markers cannot be clearly identified. Figure 5-5 shows one frame from a video made under WVGA mode with 240 frames per second. The markers towards the end are severely blurred and it is impossible to tell them apart. When tracking the red markers in the program, they intefere with the dark lines along the guide rail in the video. When the markers move across a dark line, the program often lose track of them.

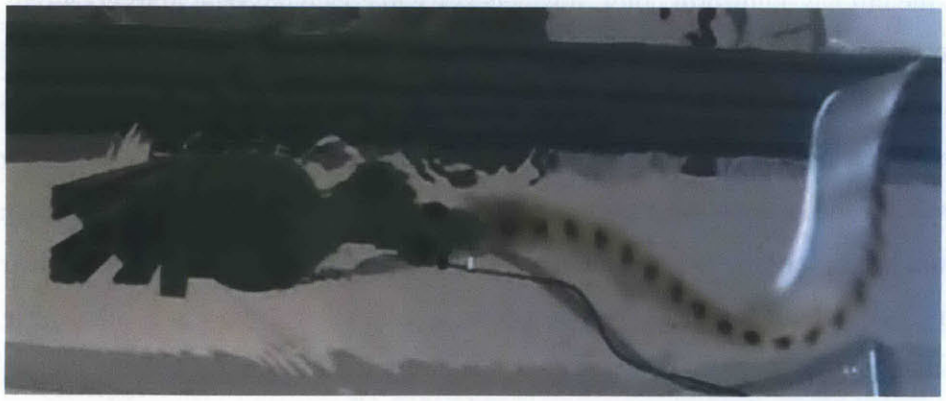

Figure. 5-5. One Frame from an Experiment Video at 240 Frames per Second

To clearly identify the markers in each frame, the frame rate must be increased. The GoPro® camera can no longer satisfy this requirement because 240 frames per second is the highest frame rate it can achieve. Therefore, a different high speed camera should be adopted to increase the frame rate. A more uniform and lighter background can help identify the markers more clearly in the videos. Alternatively, different colors of pins can be tried to figure out which color is optimal for the experiments. Red was chosen based on intuition.

CHAPTER 6

FOURTH ITERATION OF EXPERIMENTS

The three unrealized improvements discussed in Chapter 5 still need to be addressed for future experiments. Though the additional degree of freedom at the beginning of the tail is no longer required, the other two improvements must be implemented to generate better experimental results with less noise due to irrelevant factors that should be avoided as much as possible. Therefore, in this iteration of experiments, it is focused on how to reduce undesired splashes and waves and how to adopt a high speed camera with the capability of recording videos at a sufficiently high frame rate.

6.1 REDUCING SPLASHES AND VIBRATIONS

The major problems associated with the second iteration of experiments are: (1) the moving unit is too close to the water surface and thus it generates considerable splashes and waves that impede its forward motion along the guide rail; (2) the moving unit also vibrates appreciably during its forward motion, and the vibration becomes more significant when the aluminum extrusion that connects the motor housing and the carriage is extended to lower the moving unit into water; and (3) the guide rail cannot be submerged under water permanently because the steel rods on the guide rail are not resistant to corrosion due to water. The essential problem here is how to reduce undesired splashes, waves and vibrations simultaneously.

Though the steel rods on the guide rail are prone to corrosion, if the guide rail can be taken out of water easily to dry after experiments, it should no longer be a problem. As discussed in Section 5.1, it is not necessary to use a guide rail that is 4-m long, because the transient phase is very short. In addition, the OSG-25 carriage that is used in the second iteration of experiments works the best when the mounting surface faces upward. If the carriage can be arranged in the same way as it is designed to be instead of being mounted sideways as in the second iteration, it can potentially minimize the undesired vibrations during the forward motion of the moving unit. With all these factors being considered, another feasible solution has been proposed.

A shorter guide rail about 1.5-m long that can work together with the OSG-25 carriage is adopted to construct the new experimental setup. The mounting surface of the carriage faces

upward. Two triangular metal structures are used to support the guide rail on the bottom of the testing pool and elevate the guide rail from the bottom to limit the influence due to wall effects. Unlike in the second iteration of experiments, the motor housing is connected to the carriage with a 3D printed plastic piece, which decreases the total weight that the tail needs to propel. Figure 6-1 illustrates the fourth iteration of experiments.

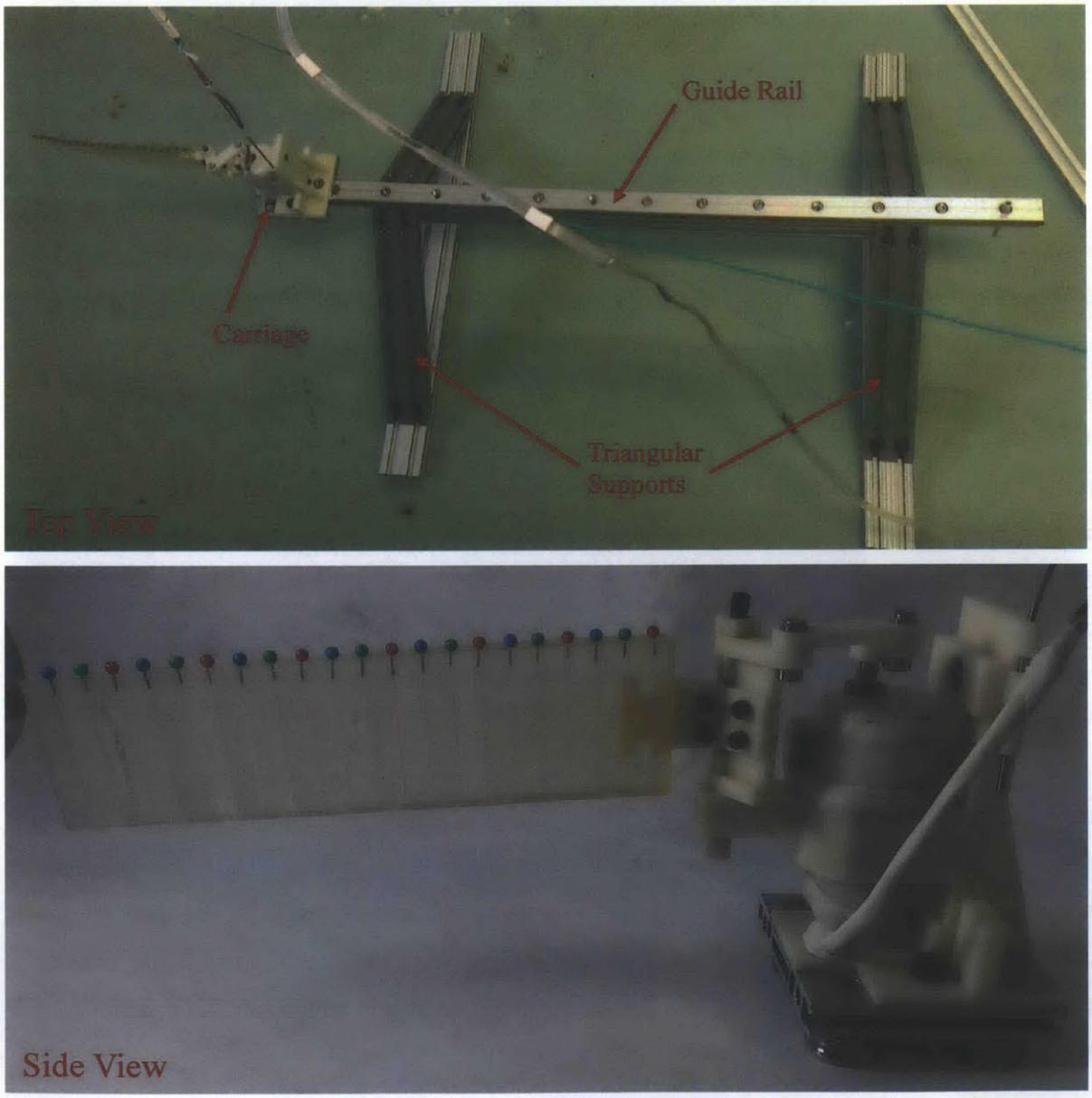

Figure 6-1. Fourth Iteration of Experimental Setup

There are several advantages of this iteration of experiments compared to the second iteration. First of all, the whole structure is more stable with less vibration than before. The mounting surface of the carriage is now facing upward instead of sideways. In such configuration the carriage is less likely to vibrate left and right while moving along the guide rail, which has been verified by a few quick experiments with various voltage input to the motor. More importantly, the entire structure sits directly on the bottom of the testing pool with more contact area than before. The angular supports are composed of wide aluminum extrusions which are less likely to deform during experiments. Secondly, the entire structure is not fixed to anything attached to the testing pool, so it is easy to take the guide rail out of water. At the beginning of an experiment, the structure should be placed into the testing pool first with a decent distance from the side wall to avoid wall effects. After the experiment is done, the structure should be taken out from the water for maintenance, mainly to dry the steel rods on the guide rail. Thirdly, because the guide rail can be taken out of water easily, it can be submerged well under water such that the moving unit can keep a distance away from the water surface. The quick experiments verify that no significant splashes and waves are generated while the tail propels the moving unit forward. Lastly, the camera can be placed above water now to record a video from the above. The markers on the tail have three different colors to differentiate adjacent markers from each other in the Tracker program. Since GoPro® camera is no longer considered sufficient to record videos at a fast frame rate, a more sophisticated high speed camera system is introduced as a replacement. The new system cannot be placed under water, so the videos must be taken from above. Thus the bottom of the testing pool, which has a more uniform color than the ceiling of the lab, becomes the background of experiment videos.

A sample experiment video can be found on YouTube for demonstration purpose [26]. A removable mechanical stop is placed at the end of the guide rail to prevent the moving unit from derailing. It takes a few seconds for the moving unit to travel from one end of the guide rail to the other. The laser sensor is not implemented in this quick experiment, so the speed data are not recorded. The speed data can be obtained from the experiment video processed in the Tracker program as well, so it is not necessary to implement the laser sensor, which cannot be submerged under water without additional measures.

6.2 HIGH SPEED CAMERA SYSTEM

Because GoPro® camera is not sufficient to record experiment videos at a fast frame rate, a more sophisticated high speed camera system is adopted for the fourth iteration of experiments. The high speed camera system consists of three major pieces of hardware: (1) conventional camera lens, (2) two 3M Camera Link® cables [27], and (3) a highly customized computer with a LabVIEW program that controls the lens and post-processes the videos. This system was originally built by Dr. Sangok Seok in the MIT Biomimetic Robotics Lab for the Cheetah project. It is slightly modified for the purpose of this project. Figure 6-2 illustrates the high speed camera setup.

Figure 6-2. High Speed Camera Setup

Figure 6-3 illustrates the camera lens along with the guide rail. The camera lens is held by a transparent plastic box which is fixed onto a metal frame constructed by a few aluminum extrusions. An extended version of the metal frame that supports the guide rail is adopted to simplify the process of placing the camera lens right above the guide rail. The position of the camera lens relative to the guide rail is adjusted by verifying the position of the guide rail in the camera view through the LabVIEW interface. The extended version allows the two triangular metal supports to be further away from each other such that they do not interfere with the mental frame that supports the camera lens during the adjustment process. A huge concern about placing the camera above water is that when the moving unit passes under the camera, the waves and ripples generated by the motion may distort the tail shape in the camera view. Therefore it is critical to eliminate the waves and ripples, and a feasible solution is to place a sheet of transparent acrylic at the water surface right under the camera lens so that it can cover the entire camera view.

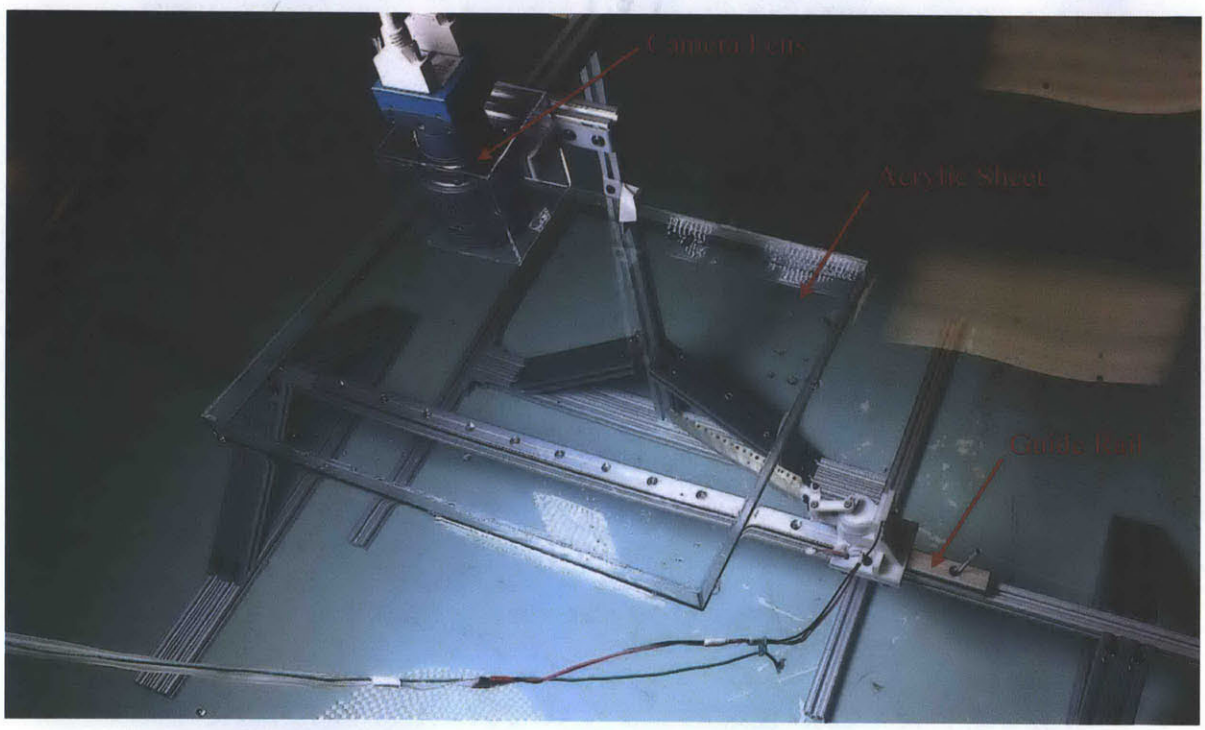

Figure 6-3. Relative Positions of the Camera Lens, Acrylic Sheet and Guide Rail

The biggest advantage of using this complicated high speed camera system is that it can record videos at a very high frame rate compared to most cameras that are readily available on the

market, including commercial high speed cameras. For example, in this application the frame rate is set to be 790 frames per second, which is 3.3 times of the highest frame rate that the GoPro® Hero 3+ Black Edition camera can provide. In addition, the view of this high speed camera system is not severely distorted compared to the view of GoPro® when it is under the WVGA mode. However, an important factor that should be considered when using this high speed camera system is that ample lighting must be provided in order to show the objects clearly. Since the frame rate is really high, without sufficient lighting the recorded videos tend to be very dark, which makes it difficult to identify and track the markers in the Tracker program. Therefore, two strong LED lights are placed close to the camera lens to make the camera view as bright as possible. Figure 6-4 shows the two LED lights relative to the experimental setup and the view from the top. To avoid the slots on the guide rail from interfering with the markers on the tail in the camera view, the section of the guide rail that is shown in the camera view is covered with blue tape, which is easy to differentiate from the markers that are in red, yellow and white. These additional measures ensure the quality of experiment videos and make it easier to track the markers in the Tracker program.

Figure 6-4. LED Lights for Ample Lighting Condition

A trade-off has to be made between the frame rate, resolution and duration of videos recorded by the high speed camera system. The reason that a highly customized computer has to be involved is that a large amount of data need to be processed and recorded quickly enough. The commercially available cameras normally do not have such computational or storage capabilities. The 3M CameraLink® cables are used to transfer the data fast and reliably to avoid noise or delay

during video recording. The hard drive and RAM on the computer are bigger than those on a normal computer. The primary concern is the duration of the video, which needs to record the entire process when the moving unit enters and leaves the camera view. The moving unit stays within the camera view for about four to five seconds, so the video duration is set to be eight seconds, which is sufficient to record the entire process. Since the total RAM is constant, the resolution is limited by the frame rate and duration. If the frame rate and resolution both have to be high while the duration is constant, the computer needs to be upgraded to keep up with the harsh requirements.

The LabVIEW program processes the data gathered by the camera lens and creates a raw file for each video, which is about several gigabytes in file size. The raw file is post processed by a different LabVIEW program to decrease its file size and change it to an avi file that can be played easily with a common video player. Since the file size is decreased to a few hundred megabytes, some information in the video is inevitably lost. The CODEC that is used to post process the videos also has to be carefully selected, because different CODECs may take different amount of time to finish the process. Sangin Park, a research scientist in the MIT Biomimetic Robotics Lab, helped to set up these LabVIEW files and select the optimal combination of frame rate, resolution and duration for the experiment videos.

A sample experiment video recorded when the voltage input to the motor was 10 V is available on YouTube for demonstration purpose [28]. Figure 6-5 shows one frame of this video as a reference. Though two strong LED lights are placed very close to the guide rail to provide ample lighting in the camera view, some area in the video still looks dark. Fortunately, it is good enough for the Tracker program to differentiate the markers from the surroundings, and the blue tape that covers the guide rail effectively avoid the slots on the guide rail from interfering with the markers. The background, which is the bottom of the testing pool, should be light blue, but in the experiment video the bottom is dark grey. Some information in the video is lost after conversion, so the quality of pictures is lower than before. As long as the markers are still clear in the video, they can be tracked automatically in the Tracker program. In fact, the Tracker program can detect the markers reliably most of the time and only minor corrections are needed to adjust the tracking region and path to keep track of the right marker in each frame. The entire experimental setup has been proven adequate to record experiment videos that can be processed in the Tracker program to extract position and even velocity information of every marker automatically with only minor

adjustments. An additional benefit of having a high speed camera system is that the linear velocity of moving unit can be measured in the Tracker program too. A characteristic point on the carriage can be tracked in the program to obtain its position and speed information. There is no need for a laser sensor to measure the speed, which is difficult to implement otherwise because the guide rail and its supporting structures are entirely submerged under water. The laser sensor is not waterproof and the light travels at a different speed under water. The waves and bubbles generated by the moving unit while traveling along the guide rail may also interfere with the light from the laser sensor, and thus the measurements may not be accurate.

Figure 6-5. A Screenshot of the Experiment Video

6.3 VERIFICATION OF CONCEPT

So far all the experiments are conducted along a guide rail, so it is not clear whether the swimming mechanism can propel a robot forward in a prescribed direction. A quick experiment to verify that

the swimming mechanism has such capability is desirable before designing a robot based on this mechanism.

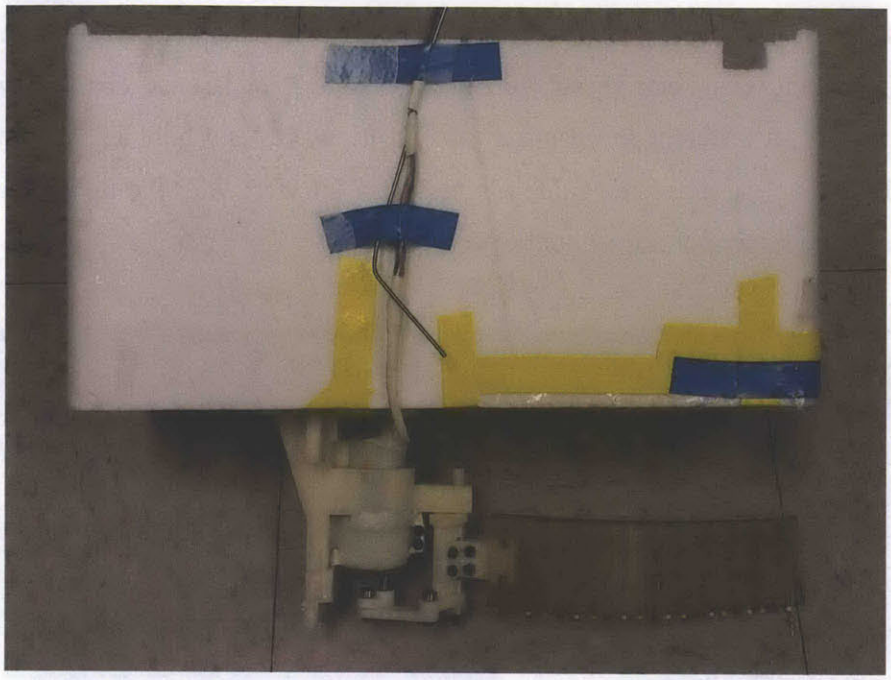

Figure 6-6. Experiment to Verify the Swimming Mechanism

Figure 6-6 illustrates the quick experiment that is used for the verification. A piece of foam is attached to the swimming mechanism with duct tapes to ensure that the entire unit can float in water freely. The foam is relatively large compared to the swimming mechanism such that it is easier to keep the unit stable in water. Therefore the mechanism is less likely to have motions in the pitch, yaw and roll directions.

An experiment video is available on YouTube [29]. The tail can propel the entire unit forward along a straight line in a prescribed direction with minor oscillations in the yaw direction, which is inevitable according to the Newton's Third Law of Motion. While the tail is oscillated by the four bar mechanism, the tail exerts a force onto the tail. Meanwhile, the tail exerts a force with the same magnitude but in the opposite direction to the four bar mechanism. The motor rotates in one direction constantly, which may cause the entire robot to spin as well. Fortunately this quick experiment proves that the swimming mechanism can propel the moving unit forward in a straight line, which is critical for making a robot based on this mechanism.

6.4 FUTURE WORK

The experimental setup has been improved to the fourth iteration, and finally most critical requirements have been met. The undesired vibration of carriage due to motor rotation is reduced significantly, and the high speed camera system can capture the tail motion clearly. The position and velocity information of every marker can be extracted from the experiment videos using the Tracker program. The data extraction process is almost automatic and only requires occasional intervention by the user to adjust the tracking region and path.

Only a few quick experiments are completed to test the experimental setup, and only one experiment video is used to extract the position and velocity information. The data are gathered to compare with the simulated results. The comparison is not yet completed by the time this thesis is submitted. The simulation discussed in Chapter 2 was not used for comparison because it is not considered to be sufficiently accurate. Josh Wiens, a Ph.D. candidate in The Hosoi Group at MIT, conducted similar research before. He made a simulation that takes into account of hydrodynamic forces using a discrete model. The simulation needs all the joint angles at each time step in order to generate the tail motion. Additional measurements, mainly the drag coefficient associated with the moving unit while it travels along the guide rail without activating the tail, are required to complete the simulation.

A slightly revised version of the experimental setup is required to measure the drag coefficient. The drag varies along with the linear speed of the moving unit along the guide rail. It is proportional to velocity squared, according to Eq. (2-2), so an intuitive way to obtain the drag coefficient is to apply a curve fit to a series of measurements of drag versus velocity squared. A force sensor is required to measure the drag on the moving unit. Most force sensors cannot be submerged under water, so it is necessary to keep the force sensor out of water while taking measurements. The simulation can be completed once the drag coefficient is obtained.

A series of experiments with various voltage input to the motor and different tails, similar to those discussed in Chapter 4, should be performed to generate sufficient experimental data for further analysis. The simulation needs to be tuned based on the experimental data in order to better guide the design process of the tail. An optimization algorithm can be applied to the simulation to generate the optimal design under specific constraints.

CHAPTER 7

UNDERWATER ADHESION MECHANISM

As discussed in Chapter 1, the existing in-pipe robots normally adopt a wheeled design to generate motion and traction. The wheeled in-pipe robots have certain limitations, for example, they can only operate in water pipes with certain diameters, the associated controlling mechanism may be complicated, and the power consumption may be high. To overcome the limitations of wheeled design, a reversible underwater adhesion mechanism is designed to generate tractions for underwater robots.

7.1 MICRO ACTIVE SUCTION CUP ARRAY (MASCA)

The goal of this part of research is to develop the cephalopod-inspired MASCA on each foot for reliable attachments. The design is inspired by cephalopods, flexible and muscular sessile suckers [30]. The principle is that a suction cup conforms to a surface and seal against it. The muscle expands the suction cup and causes the enclosed volume to increase, which lowers the internal pressure in the sessile sucker and creates a pressure differential between the interior and exterior of the sucker. This pressure differential applies to the external surface of the suction cup and pushes it against the contact surface. Therefore, the designed suction cups need to seal completely with the contact surface and have an actuator that expands the enclosed volume of the cups to induce a pressure differential. The design of the robot foot pad and a detailed view of micro active suction cups are illustrated in Figure 7-1.

The proposed design is more advanced compared to any other previously developed suction cups in terms of three major aspects: micro scale, active suction, and leakage prevention. The interior of a water pipe is a curved surface that is more difficult to conform to than a flat surface. A smaller cup correspondingly covers a smaller area and can better seal against a curved surface than a larger cup, which deforms more significantly when in contact with the same curved surface. The cups are made of Dragon Skin® FX-Pro (Smooth-on, Inc.), a type of platinum silicon rubber that is soft, elastic and resistant to tearing. This material property allows the cups to conform to surfaces with a range of various roughness. The fine-edged suction cup lip engages well with contact surface and thus seals better than a dull edge.

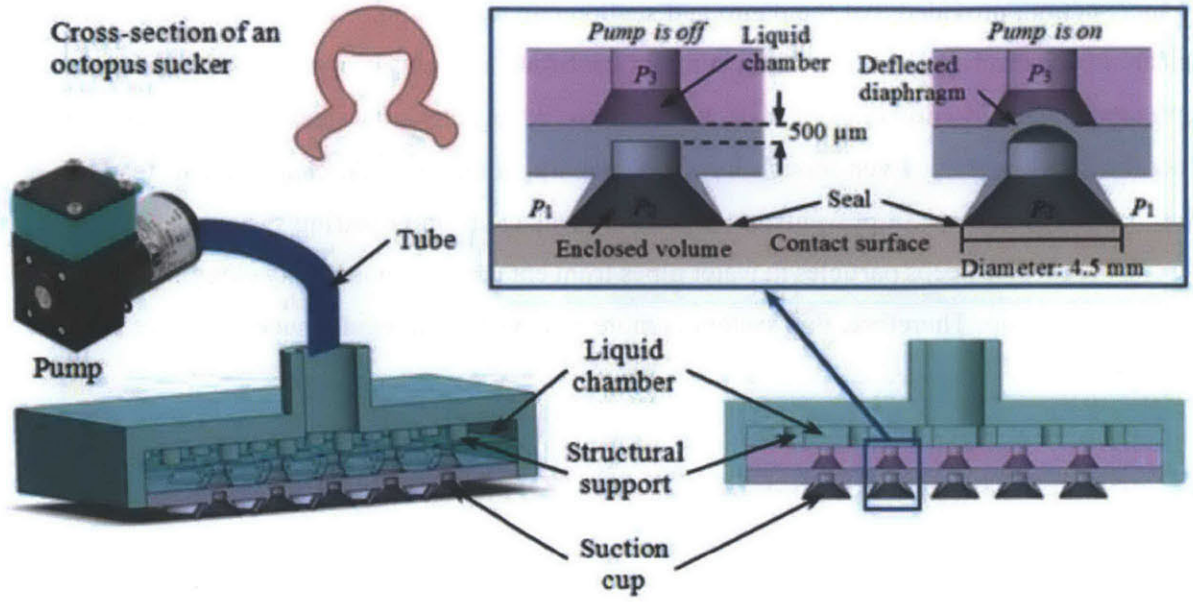

Figure 7-1. A Proof-Of-Concept Prototype

The KNF Neuberger NF 30 KPDC Micro Diaphragm Liquid Pump is selected as an actuator pump for the suction cups [31]. There is a thin diaphragm (500 μm) in each suction cup that separates the enclosed volume along the contact surface and the liquid chamber connected to the pump via a plastic tube. When the pump is off, the ambient pressure P_1, enclosed pressure P_2 and liquid chamber pressure P_3 are all equal. When the pump is activated, water is pumped out from the liquid chamber and thus decreases the suction cup pressure. P_3 becomes lower than P_2, and this pressure differential causes the diaphragm to expand upward into the liquid chamber. The enclosed volume expands accordingly. Due to the incompressibility of water, P_2 is lower than P_1. This pressure differential results in suction along the contact surface. In addition to resulting in a stronger suction than passive suction cups, another advantage of these active suction cups is that the release force can be reduced by pumping water back into the liquid chamber to deflect the diaphragm downward. This way P_2 will be increased and the suction cups can be released from the contact surface easily.

The pump can be turned off after the suction is achieved and the suction should remain even if there is a leakage at a few individual suction cups. This allows less power consumption when the robot is attached to the pipe interior. Theoretically, the pump can be connected to the enclosed volume without using the liquid chamber and diaphragm, and it will actually allow

stronger suction, provided that the pump and suction cup are the same. When an array of suction cups are in use, each individual suction cup will contribute to the system performance. Without a diaphragm, the enclosed volume of each cup is connected together, and a leakage at one cup would affect the entire system. Even though having a diaphragm and a liquid chamber will result in a lower total suction force, it prevents individual cup leakage from impairing system performance. The diaphragm also keeps particles in water pipes from entering and potentially clogging the liquid chamber and pump. Therefore, this system is more reliable than a regular suction device without a diaphragm.

7.2 FABRICATION PROCESS OF MASCA PROTOTYPE

The fabrication process is demonstrated in Figure 7-2.

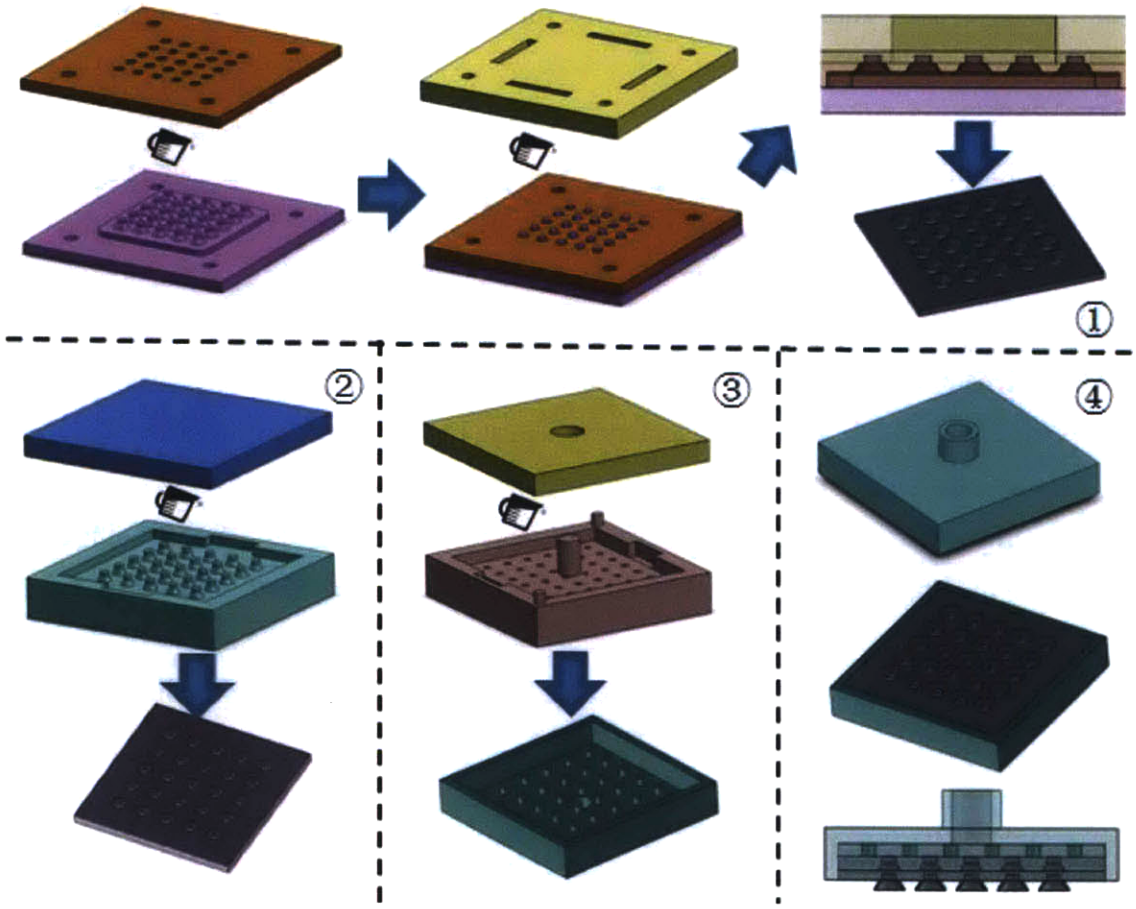

Figure 7-2. Fabrication Process of the Prototype

The first three subfigures indicate the processes to fabricate the bottom, middle and top layers, respectively. The product in each subfigure is viewed from the bottom. The last subfigure contains different views of the final product in addition to Figure 7-1. The bottom layer (grey) with the suction cups and diaphragm is made of Dragon Skin ® FX-Pro. The mold for this layer contains three pieces to achieve the intricate features on this layer. The sharp bottom rim of a suction cup engages well with contact surface and thus seals better than a dull rim. The middle layer of the prototype (pink) creates an individual liquid chamber for each suction cup. The top layer (green) creates a liquid chamber on top of all individual chambers and connects them all together. It is then connected to the liquid pump via a plastic tube. The middle and top layers are made of TAP Silicone RTV (TAP Plastics, Inc.) and also function as structural support for the foot when the pump is activated. Figure 7-3 shows the fabricated prototype.

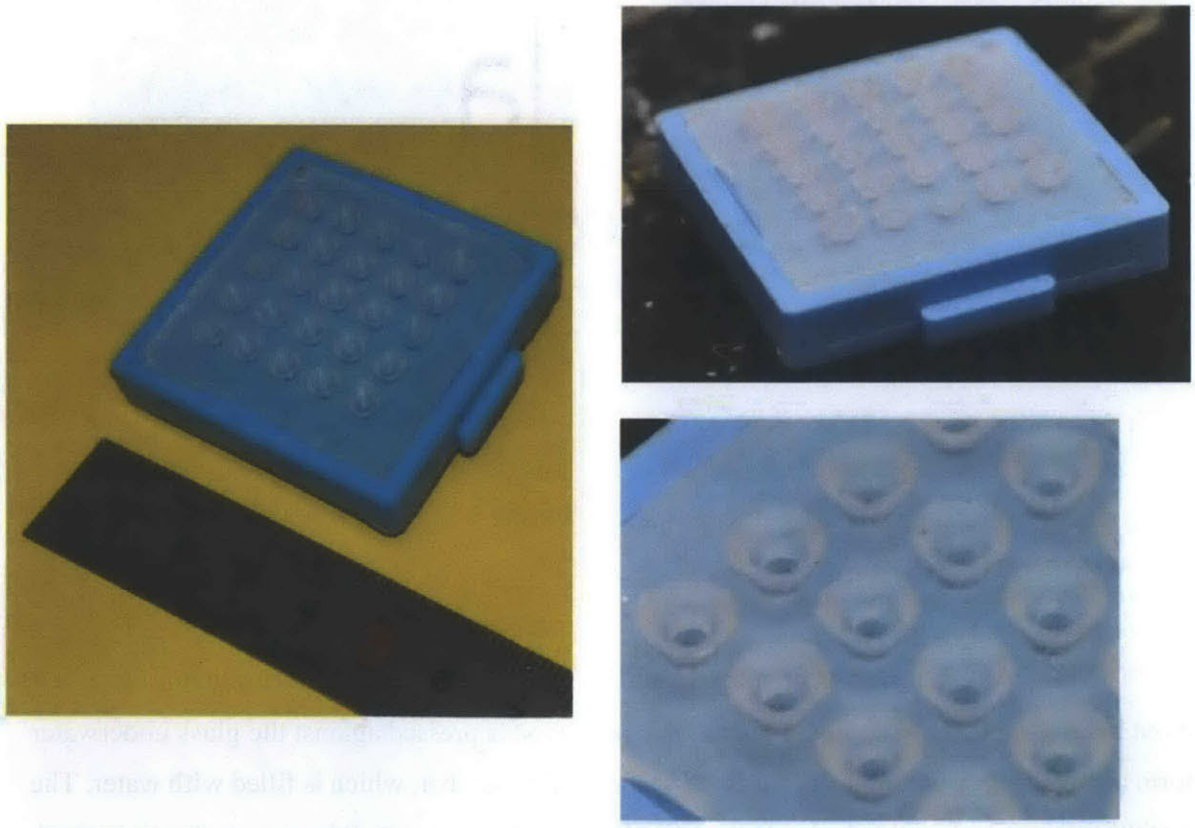

Figure 7-3. Fabricated Prototype of MASCA

7.3 TEST RESULTS AND DISCUSSION

This prototype is tested briefly on a piece of glass to obtain a rough sense of its performance and identify aspects for further improvements. At the beginning of the test, a liquid pump is connected to the liquid chamber of the suction cup array. The test is not completed successfully because the liquid chamber is too powerful. While the liquid pump sucks water out of the liquid chamber, the shape of the whole prototype is altered dramatically, shown in Figure 7-4, so the bottom of the prototype cannot remain sufficient contact with the glass surface. An alternative pump with lower suction head may be more appropriate to actuate the prototype. A small peristaltic pump is a potential option for future experiments. Meanwhile, the design of the prototype should be revised to improve the structural robustness when the prototype is actuated.

Figure 7-4. A Picture of MASCA Prototype when actuated by a Liquid Pump

Figure 7-5. Prototype lifting up a Glass

The prototype is tested again after the top layer is reinforced with more silicon rubber but without being actuated by the liquid pump. The prototype is pressed against the glass underwater to form a good seal. A tube is still connected to the liquid chamber, which is filled with water. The end of this tube is designed to be connected to a liquid pump, and now it is open to the air instead. After the prototype is in contact with the glass firmly, the free end of the tube is sealed manually to disconnect the liquid chamber from the atmosphere. When the prototype is lifted upward,

sufficient suction is achieved between the suction cups and the glass such that the glass is lifted up along with the prototype, as demonstrated in Figure 7-5. The glass weighs 90 g. When the prototype is shaken moderately with the glass attached vertically, the glass does not fall off. This case demonstrates that the prototype can withstand shear force equal to the gravity of the glass at least. Even though the enclosed volume of each suction cup is not actively expanded by exerting an external force on the diaphragm, it nevertheless becomes bigger as the shape of the suction cup skirt is changed when the prototype is lifted up. This results in a lower pressure in the enclosed volume than the ambient pressure, which induces suction. When the free end of the tube is released, the glass can be easily shaken off from the prototype. The whole experiment process is repeatable. The result is promising as it proves that the fundamental mechanism of MASCA works well on a flat and smooth surface.

7.4 FURTHER LITERATURE REVIEW

A more in-depth literature review has been done to further learn from biology and nature as well as to understand one of the limiting factors of underwater suction cups, namely the cavitation phenomenon of water.

Figure 7-6 illustrates the general anatomy of an octopus sucker [32]. Infundibulum (in) is the exposed disc-like portion of the sucker. At the center of the infundibulum is an orifice that opens into an approximately spherical cavity called the acetabulum (ac) [33]. The external surface of the infundibulum is covered by a chitinous cuticle (cc), which has a series of radial grooves and ridges on its surface. The infundibulum is encircled by a rim (r) covered with a deeply folded, loose epothelium [32].

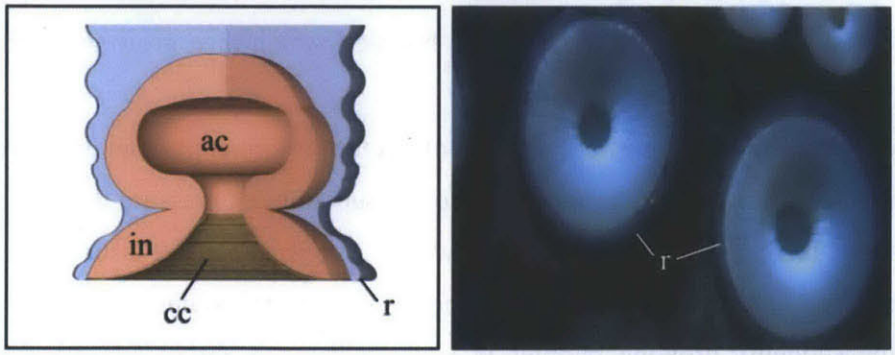

Figure 7-6. Transversal Section (Left) and Frontal Section (Right) of Octopus Sucker

A pressure differential between the ambient pressure and the pressure inside the sucker is produced by expanding the acetabulum. This sub-ambient pressure produced by the acetabulum must be transmitted under the infundibulum to the outer rim where the seal is formed. It is important to understand the mechanism of this pressure transmission. The infundibulum includes an array of radial grooves that extend from the center of the infundibulum to the rim. Also, the chitinous cuticle that covers the infundibulum has a remarkable array of denticles. When the sucker is attached to the substratum, the denticles and radial grooves form an interconnected water-filled network of spaces that can transmit sub-ambient pressure from the acetabulum all the way to the outer rim of the sucker, thereby establishing a pressure differential over the entire area of the infundibulum. The denticles also help the sucker resist shear force by enhancing the friction between the rim and the substratum [33].

The current prototype of MASCA does not have any radial grooves or denticles on the surface of the suction cup skirt, analogous to the infundibulum of an octopus sucker. Tramacere *et al.* fabricated two prototypes of underwater suction cups based on the anatomy of real octopus suckers with radial grooves implemented on the lower surface of the suction cups. They claimed that these grooves play an important role regarding the efficiency of reversible adhesion [32]. However, they did not make prototypes with smooth lower surface to compare the performance. It is worth to investigate into this problem and quantitatively measure the change in efficiency due to the implementation of such grooves and denticles.

An important factor that may limit the performance of underwater suckers is the cavitation threshold of water. Cavitation is the process of formation of the vapor phase of a liquid when it is subjected to reduced pressures at constant ambient temperature. It is one form of nucleation, defined as the extremely localized budding of a distinct thermodynamic phase. Particles suspended in water and defects on the wetted surface limit the cavitation threshold of water. The particles and defects provide nucleating sites that stabilize gas bubbles, which then grow when the pressure drops to the threshold level, initiating cavitation.

How does the cavitation threshold of water affect the performance of an underwater sucker? The attachment force of a sucker is proportional to the sub-ambient pressure that the sucker can produce. The sub-ambient pressure depends on how low the pressure inside a sucker can be. If the internal pressure goes below the cavitation threshold of water, the water inside the sucker will cavitate, and the suddenly growing bubbles in water will cause abrupt failure of the sucker.

Therefore, the cavitation threshold of water is a limiting factor of the performance of underwater suckers.

One of the biggest assumptions made in previous research is that the water cannot endure absolute pressure under 0 MPa. Tramacere *et al.* observed that their prototypes of underwater suction cups induce the cavitation of water when the sub-ambient pressure is close to 0 MPa [32]. However, Smith proved by experiment that water can withstand absolute negative pressure without cavitating. He also showed that sometimes the pressure under octopus suckers can be negative, too [34].

The cavitation threshold depends on a variety of factors, such as the liquid kind, the presence of impurities (potential nucleation sites), temperature, the kind of substrates and materials involved in the process [32]. If an experiment is conducted at room temperature with normal pure water, varying the substrate would affect the cavitation threshold of water. Crum found that decreasing surface tension decreased a liquid's cavitation threshold, which suggests that, if a surface is more easily wetted, the cavitation threshold will be lower [34] [35]. Thus, it is important to test prototypes on a carefully selected substratum that is similar to the interior of a typical water pipe.

7.5 FUTURE WORK

The prototype shows promising results of MASCA as a reversible underwater adhesion system with simple actuation. Further improvements can be done in the following areas.

Firstly, the design of prototype can be modified to improve the geometry of the suction cups. In particular, the lips should be sharper for better engagement with the substratum, which is critical when the surface is rougher than glass. The walls of suction cups can be thicker to improve the structural robustness. A problem that encountered during the experiment is that the walls of suctions are stuck to the bottom surface of the prototype when it is pressed against the glass, because the suction cups are made of soft materials (Dragon Skin® FX-Pro) that can easily bind to other objects through van der Waals force. This feature is not desirable for a reversible underwater adhesion system. The suction cups are expected to return to their original shape when not in contact with an external surface. As suggested in the previous section, it is worth to fabricate suction cups with denticles and radial grooves on the lower surface to enhance the pressure transmission to the rim as well as the friction between the lower surface and substrate. Furthermore,

the thickness of the diaphragm can be reduced to create a higher pressure differential between the enclosed volume and the liquid chamber. The diaphragm is examined under the microscope before and after the prototype is actuated by a liquid pump, as shown in Figure 7-7. It is not clear if the diaphragm undergoes significant deflection to achieve the design expectation. The angle of observation might obscure the true deformation, so a better examining method is recommended.

Secondly, some of the molds need to be modified to ensure smooth material flow into the cavity. The top and middle layers of the prototype are particularly difficult to mold due to the high viscosity of the material (TAP Silicone RTV) used. Air bubbles are usually trapped in the cavity even after being degassed for 15 minutes in a vacuum chamber. Several trials are attempted before an acceptable product can be obtained, which has wasted a significant amount of time and materials. An alternative material, for example, OOMOO® 25, can be used to replace the current one. OOMOO® 25 is advantageous compared to TAP Silicone RTV due to its lower viscosity and much shorter demold time. OOMOO® 25 only takes 75 minutes to demold, whereas TAP Silicone RTV takes six hours. OOMOO® 25 has been used in the lab to fabricate some other components. The physical properties are similar to those of TAP Silicone RTV, but there are considerably fewer air bubbles in the cured products.

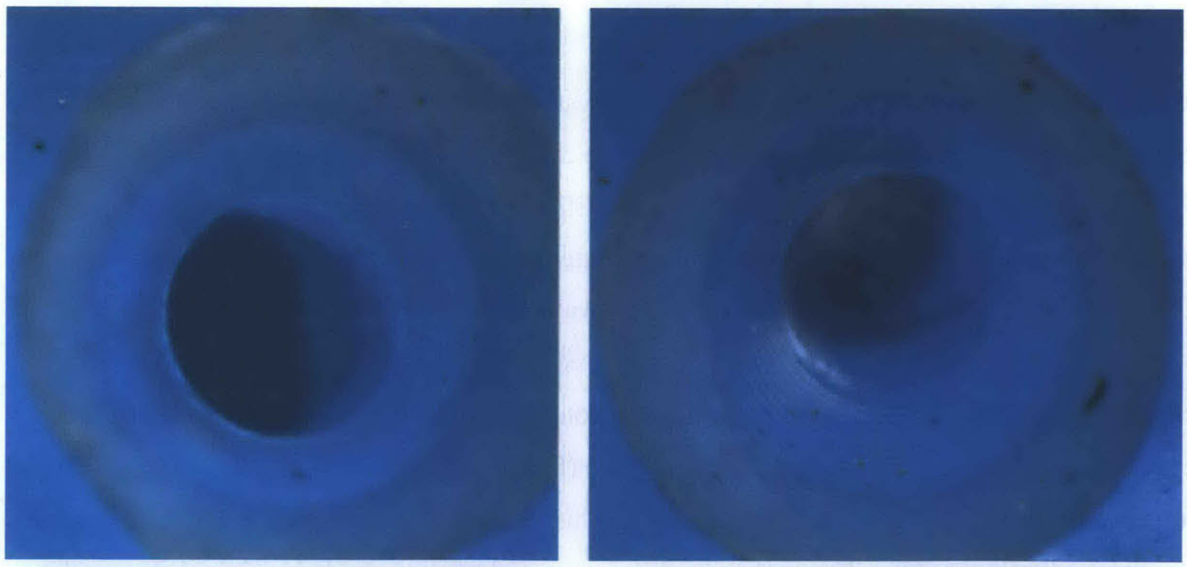

Figure 7-7. A Suction Cup before (Left) and after (Right) actuated by a Liquid Pump

Thirdly, a different actuator is recommended to replace the current liquid pump. Ideally, the actuator should be powerful enough to deform the diaphragms in the suction cups, but not alter the geometry of the prototype significantly. It is critical for the bottom layer of the prototype to maintain good contact with the adhered surface. A small peristaltic pump is a potential candidate for the replacement.

CHAPTER 8

FIRST GENERATION OF ROBOT

A bio-inspired legged pipe-crawling robot is developed to address the aforementioned limitations in Chapter 1 and to ensure functionalities specific to the WPN. A legged robot can potentially have a small cross-section relative to the pipe interior and operate along one side of the pipe interior instead of operating at the pipe center, where the flow rate is the highest. This advantage may allow a legged pipe-crawling robot to be more maneuverable inside a pipe and more accommodating to different sizes of pipes than a wheeled robot.

8.1 BACKGROUND AND INTRODUCTION

Figure 8.1 illustrates the concept drawing of the bio-inspired legged pipe-crawling robot.

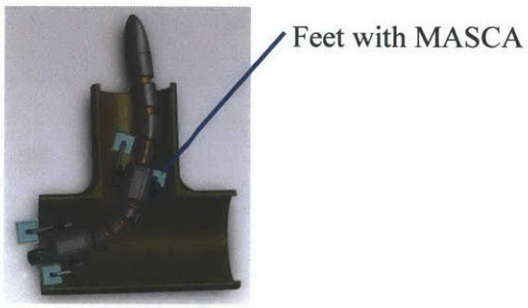

Figure 8-1. A Concept Drawing of the Bio-Inspired Legged Pipe-Crawling Robot

The design requirements of this legged in-pipe robot include:

(a) Waterproof and not contaminate clean water during operation: All the electric components will be enclosed in the robot body, which has a limited number of kinetic parts to propel the robot. The joints between the body and kinetic parts should prevent water from entering the body. The material that is in contact with water directly should not release any contaminants.

(b) High maneuverability in WPN with various pipe diameters and surface roughness: The robot will employ an underwater adhesion system that allows the robot to attach and detach from a surface repeatedly and reliably. The underwater adhesion system will supply

sufficient traction for the robot to operate in turbulent water flow of up to 2 m/s by using a liquid pump to control an array of micro active suction cups on soft foot pads. The robot will be able to turn up to 90 degrees in the lateral plane.

(c) Self-contained with power generation device: The robot will carry a battery and a power generation device. The robot will be designed to be energy efficient, and it can generate power to charge the battery with water flows in the pipe when the battery is low.

The design of the first prototype of the robot is illustrated in Figure 8-2. The purple section in the background is part of an 8-in diameter pipe, which is the standard size for developing the first prototype.

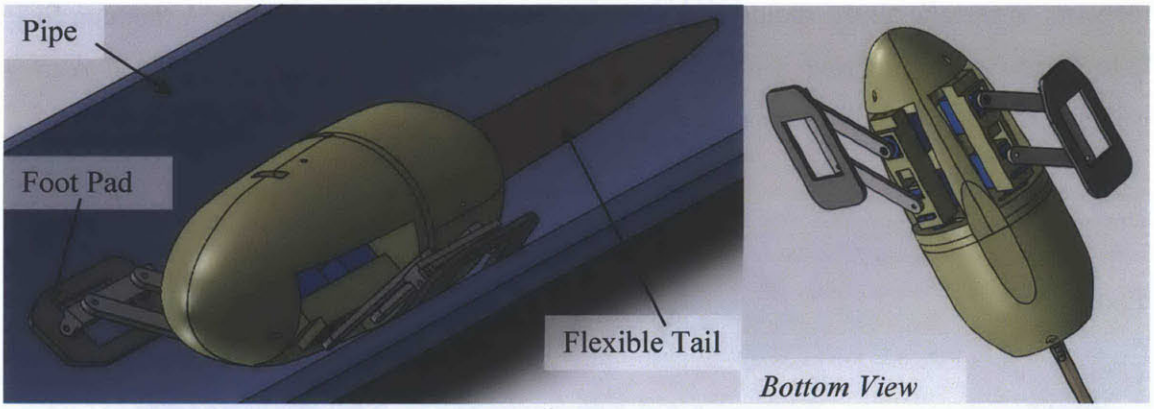

Figure 8-2. First Generation of the Robot Design

The two primary features expected to be realized on the first prototype of the robot are: (1) a crawling mechanism with a four bar linkage, and (2) a swimming mechanism with a flexible tail. Most of the rigid components on this prototype are 3D printed and the servos are the common types that can be bought off the shelf easily.

8.2 CRAWLING MECHANISM

A detailed illustration of the crawling mechanism is shown in Figure 8-2. The crawling mechanism has two active degrees of freedom, indicated by the blue arrows in the figure. The first active degree of freedom is to control the foot pads to move back and forth along the moving direction of the robot, which is normally parallel to the centerline of the pipe. The foot pads are thus moved

parallel to the robot body. This degree of freedom is realized by using a four bar linkage controlled by a micro servo (Servo 1), shown in Subfigure 2 of Figure 8-2. The second active degree of freedom is to move the foot pad up and down with respect to the interior surface of the pipe that the robot is in contact with, as shown in Subfigure 3. This degree of freedom is controlled by Servo 2, which spins about an axis that is fixed to the robot body. Each foot pad is free to rotate with respect to the bar it is connected with. This degree of freedom, indicated by the orange arrow in Subfigure 3, allows the foot pad to adapt to various curvatures of pipes.

The servos used in this prototype are Tower Pro SG92R Micro Servos. They are inexpensive, compact and able to deliver sufficient torque for the application. There are water-proof versions which can be adopted in the next version of the prototype for underwater testing.

The MASCA has not been implemented onto the first prototype yet. It would require extensive work to remake all the molds on a CNC machine to fabricate the MASCA that can fit with the foot pad. Several improvements should be addressed for the next version of MASCA to achieve a more reliable reversible underwater adhesion system.

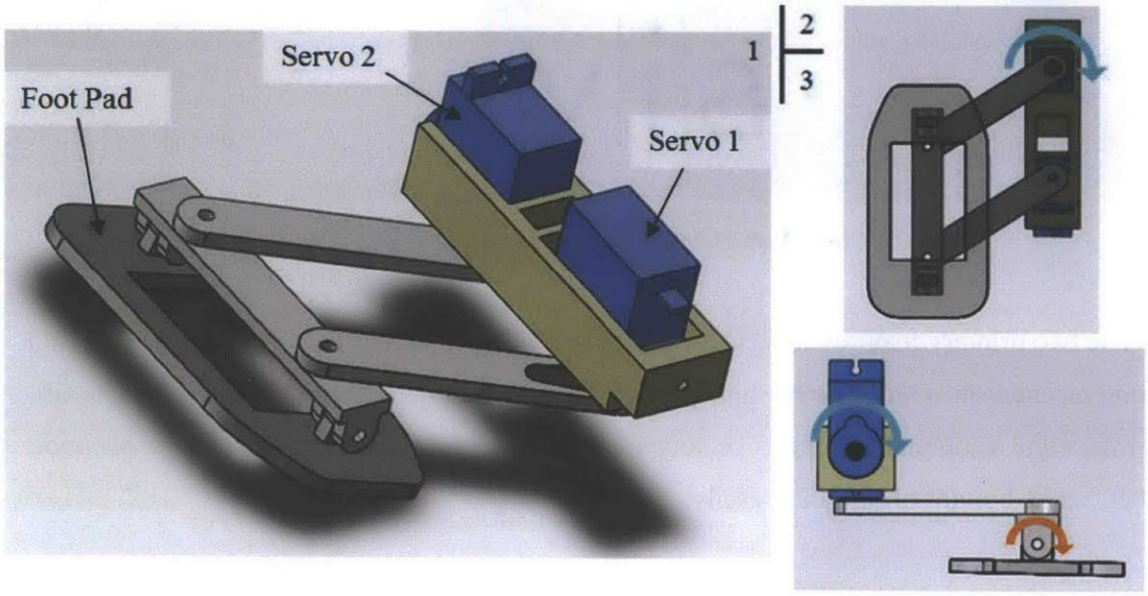

Figure 8-2. Crawling Mechanism

8.3 SWIMMING MECHANISM

A detailed illustration of the swimming mechanism is shown in Figure 8-3.

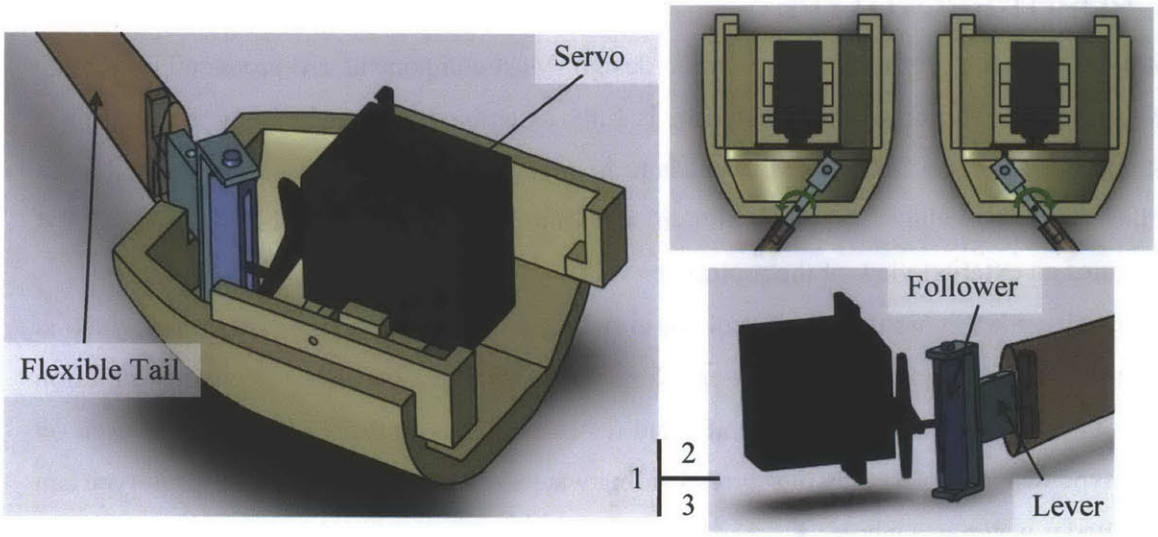

Figure 8-3. Swimming Mechanism

The swimming mechanism [36] basically comprises of a Scotch yoke and lever mechanism driven by a continuous servo (SpringRC SM-S4303R) to control the motion of a flexible tail made out of polymers. The servo and follower form the Scotch yoke, which is a common approach to convert continuous one directional rotation into translational oscillation. The lever rotates around an axis fixed to the robot body shown as the yellow part in the figure. Figure 8-3 (2) demonstrates the range of motion of the lever. Figure 8-3 (3) provides a more detailed view of the Scotch yoke and lever mechanism. A pin connects the follower and the servo horn.

The flexible tail is molded over the lever to produce an integral part. The tail is designed to be flexible enough to transmit the oscillation through the longitudinal direction. The tail motion is in a wave form from the lever to the end of the tail. The tail should be able to support its own weight when in water.

The Scotch yoke and lever mechanism is not the only option to oscillate the tail. Connecting the tail directly to the servo and rotating the servo back and forth may be an alternative method. However, the speed of a servo may limit the maximum frequency that can be generated by the mechanism. The maximum speed of the servo is 50 RPM, equivalent to 300 degrees per second. If the tail is expected to quickly oscillate with large amplitude, driving a servo back and forth may not be feasible to achieve the goal.

8.4 ROBOT PROTOTYPE

A prototype has been fabricated based on the design. Most components are produced by the 3D printer in the lab. The crawling mechanism is fully assembled. The swimming mechanism is almost completed except that a tail still needs to be molded. The five servos are supposed to be controlled by one Arduino board, which is not embedded into the robot yet. Figure 8-4 demonstrates an external view of the prototype.

An algorithm is written to control the crawling mechanism, and an experiment video is available on YouTube to demonstrate the crawling mechanism [37]. Once the underwater adhesion system is improved, it will be implemented and tested on this prototype. All the servos used on this prototype will be replaced by the corresponding water-proof versions so that the prototype can be tested under water as a whole.

Figure 8-4. First Generation of the Robot Prototype

CHAPTER 9

SECOND GENERATION OF ROBOT

The main feature of the first generation of robots is the crawling mechanism. The swimming mechanism involves a servo motor which is not ideal for generating high frequency oscillation. The propulsion mechanism that is introduced in Chapter 2 through Chapter 5 is implemented in the second generation of robot, which has a simplified version of crawling mechanism. The primary purpose of the second generation is to prove that the swimming mechanism can propel a robot that is not constrained to a guide rail or any other structure forward reliably. The robot has some additional features, for example, a pair of rotating legs that can help steer the robot while it is swimming in water. The robot can crawl on the ground with the rotating legs. It also carries a mini camera that can record a video while the robot operates in water pipes.

9.1 ROBOT DESIGN

Figure 9-1 illustrates the design of the second generation of robot.

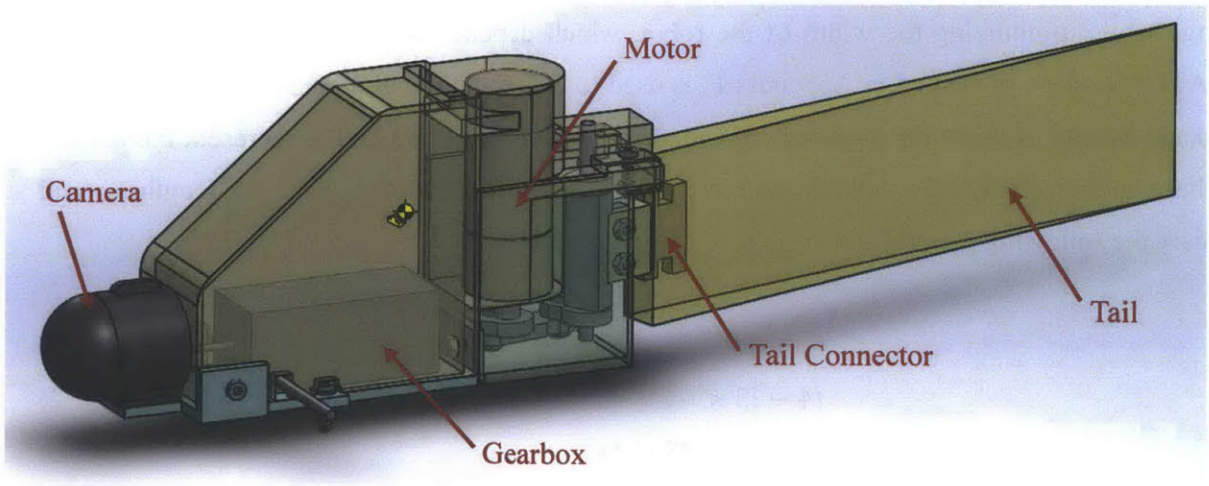

Figure 9-1. Second Generation of the Robot Design

To demonstrate the critical components clearly, the plastic cases are shown semi-transparent. The legs are not shown in the figure. Most components are fabricated on the 3D printer. The camera is placed at the beginning of the robot to record a video or take pictures while the robot operates in a water pipe.

The second generation of robot is designed based on the propulsion mechanism discussed in Chapter 2 through Chapter 5. To minimize the cross-sectional area of the robot and thus the drag on the robot when swimming in water, a different type of motor is adopted in the robot design. One of the reasons that the original motor was adopted in the experimental setup is because that type of motors were readily available in the lab. The 9.7:1 Metal Gearmotor 25DX48L mm HP with 48 CPR Encoder is chosen for the robot design [38]. The original motor is 36.80 mm in diameter, whereas the new motor is merely 24.75 mm in diameter. The maximum width of the robot is thus reduced to 36.75 mm. The specifications of the motor are different than before, but it is expected to drive the tail smoothly along with the four bar linkage with revised dimensions. The motor should be able to deliver sufficient power to drive the tail, and the speed of rotation is controlled by adjusting the voltage input to the motor.

The four bar linkage is modified to minimize the cross-sectional area as well. The rocker range is designed to be around 60 degrees from one side to the other, as defined in Figure 3-5. It is not intuitive how to set up the dimensions of the four bar linkage to achieve this desired rocker range while minimizing the width of the robot, which depends on the length of the rocker. A MATLAB script, presented in Appendix F, is used to find the optimal dimensions of the four bar linkage instead of using the trial and error method. Assume $l1$, $l2$, $l3$ and $l4$ represent the lengths of base, rocker, crank and coupler, respectively. To form a crank-rocker linkage, the lengths should satisfy the following general constraints:

$$l1 + l3 < l2 + l4 \tag{9-1}$$

$$l4 - l3 < l1 + l2 < l3 + l4 \tag{9-2}$$

$$l3 < l4 \tag{9-3}$$

The maximum and minimum values of the angle between the rocker and bases, represented as *aMax* and *aMin*, respectively, are calculated as follows:

$$\text{aMax} = \arccos\frac{(l3+l4)^2-(l1^2+l2^2)}{-2\cdot l1\cdot l2} \tag{9-4}$$

$$\text{aMin} = \arccos\frac{(l4-l3)^2-(l1^2+l2^2)}{-2\cdot l1\cdot l2} \tag{9-5}$$

The half rocker range is thus calculated by

$$\frac{1}{2}\text{RockerRange} = \frac{\text{aMax}-\text{aMin}}{2} \tag{9-6}$$

The lengths of rocker and crank ($l2$ and $l3$) need to be prescribed at the beginning of the MATLAB script based on a reasonable estimation according to the desired dimension of the robot. The script conducts a parameter sweep for the lengths of base and coupler ($l1$ and $l4$) and finds the minimum rocker range. The dimensions of the four bar linkage in the original propulsion mechanism were determined in SolidWorks based on manual inspection. This MATLAB script greatly improves the efficiency of determining the dimensions. In the end, the rocker range is set to be 67.5 degrees, and the total width of the robot is 36.75 mm.

The underwater adhesion system is not implemented on the second generation of robot, otherwise the robot may be overly complicated. The primary concern is to test if the propulsion system is truly capable of driving a robot forward in water following a prescribed path, which is a straight line. Though a quick experiment, discussed in Section 6.3, proves that the propulsion system is promising to achieve this requirement, a small body may cause trouble for the robot to maintain stability if the tail oscillates fast. In addition, it may be challenging to adjust the buoyancy of the robot when multiple materials and components are involved. A Tamiya® Universal Gearbox (Item 70103) with a worm gear is contained in the front body of the robot to drive a pair of rotating legs [39]. A worm gear allows a relatively high gear ratio, which slows down the speed of rotation while increase the output power from the shaft. It is suitable for driving the legs which are used for crawling. The leg design is inspired by Salamandra Robotica [40]. The legs have not been designed and implemented by the time this thesis is submitted.

One of the major purposes of this robot is to inspect the internal conditions of water pipes. Many factors need to be taken into account in order to construct an underwater vision system to record videos or take pictures reliably while the robot moves around in water pipes. The camera installed on the robot is mainly for demonstration purpose for now. It proves that the robot has the

capability of carrying a compact camera with wireless communication. If the camera is not fully submerged under water, the camera can be used to monitor the surroundings in real time, and a user can view the pictures and videos on a computer easily. In the future it is critical to set up a more reliable camera system to inspect the internal conditions of water pipes, but for now the propulsion and crawling mechanisms deserve more attention.

The front body of the robot is empty besides the gearbox. The batteries can be carried on board to power the motor that drives the four bar linkage and the tail as well as the motor in the gearbox. Additional weights can be embedded to adjust the position of center of mass and buoyancy.

The four bar linkage is enclosed by a plastic case to avoid contact with surrounding water directly. While the robot operates, the four bar linkage moves quickly in water and generates undesired turbulence which may cause significant drag. The plastic case prevents water from contacting the four bar linkage. A piece of rubber is needed to seal the gap between the plastic case and tail, which oscillates quickly during operation. The rubber is not shown in the CAD model in Figure 9-1.

9.2 ROBOT PROTOTYPE

A robot prototype is fabricated based on the design shown in Figure 9-1. The gearbox, motor and camera are all implemented on this robot. The batteries are not carried on board. Instead the motors are powered by an external power supply through long wires. The tethered version of prototype has limited range of motion, but it is sufficient for testing purpose. Figure 9-2 illustrates the robot prototype without the rotating legs. It is an external view of the entire robot prototype. The gap between the plastic case and the tail is not sealed with a piece of rubber yet. Figure 9-2 (b) demonstrates the gearbox on the bottom piece of the robot. The gearbox is secured onto the bottom piece with two screws. Figure 9-2 (c) demonstrates the four bar linkage and the motor. The coupler is cut out of a piece of stainless steel with a water jet machine. It is stronger and thinner than a 3D printed plastic piece. The 18-8 Stainless Steel Nylon-Insert Hex Locknuts (2-56 Thread Size, 1/4" Width, 9/64" Height, McMaster-Carr® Part No. 91831A002) and Low Profile 18-8 Stainless Steel Shoulder Screws (Slot Drive, 3/32" Diameter X 3/16" LG Shoulder, 2-56 Thread, McMaster-Carr® Part No. 99154A394) are used for connections. The smaller thickness of the stainless steel compared to plastic allows the shoulder screws to insert into the nylon layer of the locknuts to

ensure good connections. The coupler might be broken if it were 3D printed with the same thickness.

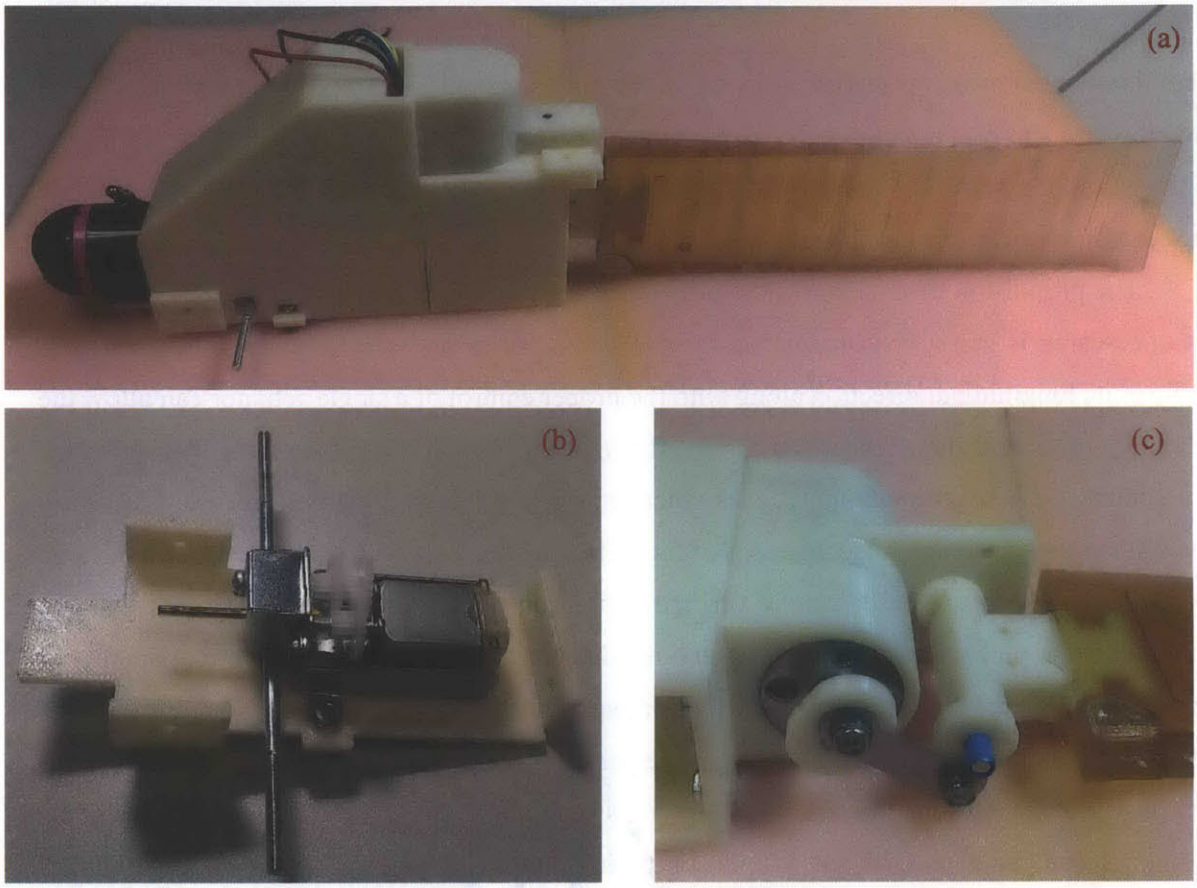

Figure 9-2. Second Generation of the Robot Prototype

A series of long wires is needed to power the robot with a stationary power supply that is placed out of the testing pool. The robot needs to be sealed with Sugru® to ensure it is waterproof before testing in water. No experiments have been done on this prototype by the time this thesis is submitted.

CHAPTER 10

CONCLUSIONS AND FUTURE WORK

The ultimate goal of this research project is to develop an underwater pipe inspection robot with both crawling and propulsion mechanisms. Though two robot prototypes were developed during the two years of research on this project, future improvements are still needed to develop a reliable robot that can be deployed to inspect water pipes.

The propulsion mechanism is the primary concern of this research. The hypothesis of this part of research is that a continuous passive compliant tail structure with an optimized stiffness profile in its longitudinal direction along with the proper control of a single actuator can allow the undulatory motion of this mechanism to resemble real fish swimming locomotion. This approach is in contrast to conventional approaches where multiple joints are actuated to create traveling waves to emulate propulsion mechanisms of fish. The goal is to verify this hypothesis and develop a propulsion mechanism based on the verified hypothesis to drive an underwater robot that can operate in water pipes. Chapter 3 to Chapter 6 are dedicated to describe the developing process of such a propulsion mechanism. Four iterations of experiments were developed in total to verify the hypothesis, take measurements and improve the performance of the propulsion mechanism. It has been proven that a continuous passive compliant structure driven by a DC motor through a four bar linkage can generate sufficient propulsion to drive a moving unit forward along a guide rail. The experiments with a simple prototype, discussed in Section 6.3, has proven that the propulsion mechanism is promising to drive a robot forward along a prescribed path without a guide rail. The propulsion varies along with a number of factors, including the geometry of the passive compliant structure. Quantitative measurements were taken using the second iteration of experiments, based on which it is proven that the stiffness profile in the longitudinal direction is one of the critical factors that affects the performance of the propulsion mechanism. However, it is not intuitive how to optimize the stiffness profile to improve the performance, so it is necessary to develop a reasonable simulation that guides the design process of the propulsion mechanism. The focus of this simulation is to investigate how the geometry and material properties, mainly elasticity, of the compliant structure affect its performance. Though the overall performance also depends on the form of actuation, which can be varied in the simulation as well, for now the actuation in the

simulation is matched with that in the experiment to compare the simulated and experimental results. The fourth iteration of experiments, discussed in Chapter 6, involves a high speed camera system that can record videos during experiments with an adequately high frame rate to capture the detailed motion of the compliant structure. A series of evenly spaced characteristic points are selected along the compliant structure which are tracked in a computer program called Tracker that can extract position and velocity data of each point based on an experiment video. The setup in the fourth iteration of experiments is capable of producing high-quality experiment videos that are acceptable to the Tracker program for automatic tracking with minor interventions from the user during the tracking process. The extracted kinematic data are used to compare with the simulated results for verification. Once the simulation is tuned to match with a few experiments, it can be used to guide the design of compliant structure in the future. Namely, the user can manipulate the parameters in the simulation to predict the outcome instead of implementing the changes to the experiments directly. Making physical changes to the prototype is more time-consuming than testing in simulation, which is why a simulation is often times desired for the development of a robot. Though no quantitative comparison between the simulation and experiment is completed by the time this thesis is submitted, it is among the top priorities of the extension of this research. Even if the simulation discussed in Chapter 2 is proven to be not sufficiently accurate to guide the design process of the compliant structure, existing simulation developed by other researchers may be used as replacements. Josh Wiens, a Ph.D. candidate in The Hosoi Group at MIT, has agreed to provide assistance for this research project. He is well experienced in developing simulations for similar swimming mechanism.

The reversible underwater adhesion mechanism, discussed in Chapter 7, is another critical component of the underwater pipe inspection robot that is under development. The goal of developing a reversible underwater adhesion mechanism is to provide adequate traction to various surfaces while the robot operates in water. Many existing pipe inspection robots adopt wheels to generate traction, and in most cases they can only adapt to certain pipe sizes. The reversible underwater adhesion mechanism would allow a robot to operate in water pipes with different sizes. A micro active suction cup array (MASCA) is developed as a prototype. Each MASCA consists of a series of micro suction cups made of soft elastic materials, namely Dragon Skin® FX-Pro, and a micro liquid pump that actuates all the suction cups on the same panel. In each suction cup there is a layer of rubber that prevents leakage at individual cups from ruining the performance of

the entire array. The entire array is fabricated with a series of carefully designed molds. A prototype is able to lift up a piece of glass that is 90 g. Several improvements should be made to generate a more reliable version of MASCA. The geometry of individual suction cups can be modified to enhance their engagement with various types of surfaces. The material of the structural support can be more rigid to improve the structural robustness of the entire MASCA while being actuated. A different type of actuation is recommended to better suit the needs of MASCA.

Two generations of robot prototypes have been developed. The first generation is to demonstrate the feasibility of a crawling mechanism, which consists of a pair of legs controlled by four mini servos in total. The propulsion mechanism on the first generation of robot is for demonstration purpose only. The reversible underwater adhesion mechanism is expected to be implemented onto the crawling mechanism in the future. The second generation is to prove that the propulsion mechanism, as discussed in Chapter 3-5, is sufficient to drive an underwater robot forward along a prescribed path. The design of the propulsion system was modified to limit the overall width of the robot so that the drag is limited as a result. The crawling mechanism is not implemented on the second generation of robot. Though the prototype has been built before this thesis is submitted, it still needs to be tested underwater to verify that the propulsion mechanism is suitable for driving a robot forward. Measurements should be taken during the experiments for further analysis to improve the performance of the system.

In conclusion, during the two years of this research project, a few critical topics have been explored for the development of an underwater pipe inspection robot. The prototypes of the propulsion and underwater adhesion mechanisms seem to be promising for actual implementation, though further improvements of these two mechanisms are still needed. Generating propulsion with a passive compliant structure with an optimized stiffness profile driven by a single actuator is an innovative approach that has tremendous academic value as well as potentially significant impact on the design of underwater vehicles. The reversible underwater adhesion mechanism is also a long-time research topic with profound practical value that deserves more attention from researchers and engineers. It is highly recommended that more effort will be devoted to extend the research on these two topics in the future.

REFERENCES

[1] Wang, Z., Hang, G., Li, J., Wang, Y., and Xiao, K., A micro-robot fish with embedded SMA wire actuated flexible biomimetic fin, *Sensors and Actuators A: Physical*, 144 (2008) 354-360.

[2] Yu, J., Wang, S., and Tan, M., A simplified propulsive model of bio-mimetic robot fish and its realization, *Robotica*, 2005, volume 23, pp. 101-107.

[3] Hu, H., Biologically Inspired Design of Autonomous Robotic Fish at Essex, *Proceedings of the IEEE SMC UK-RI Chapter Conference*, 2006.

[4] Suzumori, K., Miyagawa, T., Kimura, M., and Hasegawa, Y., Micro Inspection Robot for 1-in Pipes, *Mechatronics, IEEE/ASME Transactions on* , vol.4, no.3, pp.286-292, Sep 1999.

[5] Changrak, C., Chatzigeorgiou, D., Ben-Mansour, R., and Youcef-Toumi, K., Design and Analysis of Novel Friction Controlling Mechanism with Minimal Energy for In-pipe Robot Applications, Proc. of *IEEE International Conference on Robotics and Automation* , 14-18 May 2012, St. Paul, MN, USA, pp.4118-4123.

[6] Jung-Sub, L., Se-Gon, R., Do Wan, K., Hyungpil, M., and Hyouk, R.C., In-pipe Robot Navigation Based on the Landmark Recognition System using Shadow Images. *Proc. of the IEEE International Conference on Robotics and Automation.* 12 – 17 May 2009, Kobe, Japan, pp. 3441-3446.

[7] Peng, L., Shugen, Ma., Bin, L., Yuechao, Wang., and Yunhui, Liu., Self-rescue Mechanism for Screw Drive In-pipe Robots, *Proc. of IEEE/RSJ International Conference on Intelligent Robots and Systems,* 18-22 October 2010, pp.2843-2849.

[8] Zhang, Y., and Yan, G., In-pipe Inspection Robot with Active Pipe-diameter Adaptability and Automatic Tractive Force Adjusting, *Mechanism and Machine Theory,* vol. 42, issue 12, pp. 1618-1631, 2007.

[9] GE Industrial, Internal Robotic inspection Tool for Unpiggable Pipe Inspections, May/June 2012, Retrieved August 1, 2014, from http://www.geindustrial.com/publibrary/checkout/Robotics?TNR=Articles|Robotics|generic

[10] PureRobotics – Robotic Pipeline Inspection, Retrieved August 1, 2014, from http://www.puretechltd.com/services/robotics/

[11] Asada, H., MIT 2.12 Lecture Notes Chapter 7 Dynamics, 2013.

[12] Crank Rocker Design, Retrieved August 1, 2014, from http://www.tcnj.edu/~EXOLEG/pictures.htm

[13] Pololu, 19:1 Metal Gearmotor 37Dx52L mm with 64 CPR Encoder, Retrieved August 1, 2014, from http://www.pololu.com/product/1442

[14] Experiment Video: http://youtu.be/D4TTB7dZJyQ

[15] LM76, Speed Demon OSG Type, Retrieved August 1, 2014, from http://www.lm76.com/speed_rail_osg.htm

[16] Micro-Epsilon, Compact and Reliable Laser Distance Sensor, Retrieved August 1, 2014, from http://www.micro-epsilon.com/displacement-position-sensors/laser-distance-sensor/optoNCDT_ILR_1030_1031/index.html

[17] Pololu, ACS714 Current Sensor Carrier -30A to +30A, Retrieved August 1, 2014, from http://www.pololu.com/product/1187

[18] GoPro® HERO3+ Black Edition, Retrieved August 1, 2014, from http://gopro.com/cameras/hd-hero3-black-edition

[19] Experiment Video: http://youtu.be/54I6yzBrQjg

[20] Experiment Video: http://youtu.be/6hDOhRvNBd4

[21] Wikipedia, Cost of Transport, Retrieved August 1, 2014, from http://en.wikipedia.org/wiki/Cost_of_transport

[22] Tucker, V.A., The Energetic Cost of Moving About, *American Scientist*, vol. 63, No. 4, pp. 413-419, July-August 1975

[23] The Physics and Biomechanics of Swimming, Retrieved August 1, 2014, from http://swimright23.webs.com/dragandresistance.htm

[24] Experiment Video: http://youtu.be/JYmS1c2bmqI

[25] Douglas Brown, Tracker, Video Analysis and Modeling Tool, Retrieved August 1, 2014, from http://www.cabrillo.edu/~dbrown/tracker

[26] Experiment Video: http://youtu.be/qh_CpIVHvtQ

[27] 3M Camera Link® and Mini-Camera Link® Applications, Retrieved August 1, 2014, from http://solutions.3m.com/wps/portal/3M/en_US/Interconnect/Home/Solutions/MachineVision/

[28] Experiment Video: http://youtu.be/xQaKgcTgXJg

[29] Experiment Video: http://youtu.be/qijsqikd--g

[30] Smith, A. M., Cephalopod Sucker Design and the Physical Limits to Negative Pressure, *Journal of Experimental Biology,* vol. 199, pp. 949–958, 1996.

[31] KNF Neuberger NF 30 KPDC Micro Diaphragm Liquid Pump, Retrieved August 1, 2014, www.knfusa.com/?eID=downloadDialog&file=fileadmin/user_upload/PDF/US/Data_sheets/Updated_Datasheets/KNFUSA_NF1-25.pdf

[32] Tramacere, F., Beccai, L., Mattioli, F., Sinibaldi, E., Mazzolai, B., Artificial Adhesion Mechanisms inspired by Octopus Suckers, *2012 IEEE International Conference on Robotics and Automation*, 14-18 May, 2012, RiverCentre, Saint Paul, Minnesota, USA.

[33] Kier, W. M., and Smith, A. M., The Structure and Adhesive Mechanism of Octopus Suckers. *Integrative and Comparative Biology*, 2-6 January, Anaheim, CA, USA, pp.1146-1153.

[34] Smith, A.M., Negative Pressure Generated by Octopus Suckers: A Study of the Tensile Strength of Water in Nature, *Journal of Experimental Biology*, 1991, Vol. 157, pp. 257-271.

[35] Crum, L.A., Tensile Strength of Water, *Nature*, 8 March 1979, Vol. 278, pp. 148-149.

[36] Yu, T.S., Lauga, E., and Hosoi, A.E., Experimental Investigation of Elastic Tail Propulsion at Low Reynolds Number, *Physics of Fluids*, 7 September 2006, 18.091701, pp. 1-4.

[37] Experiment Video: http://youtu.be/hm3rhlXQT5o

[38] Pololu, 9.7:1 Metal Gearmotor 25Dx48L mm HP with 48 CPR Encoder, Retrieved August 1, 2014, http://www.pololu.com/product/2271

[39] Pololu, Tamiya 70103 Universal Gearbox Kit, Retrieved August 1, 2014, http://www.pololu.com/product/69

[40] EPFL STI IBI BIOROB, Salamandra Robotica, Retrieved August 1, 2014, http://biorob.epfl.ch/salamandra

APPENDIX A

```
close all;
clear;
clc;

name = 'ThreeLink';

dim = 7;     % Number of links
pts = 11;    % Number of sample points along each link

% Initiate variables
syms t x y dx dy ddx ddy real
th = sym('th%d', [dim 1]);      % Joint angles
dth = sym('dth%d', [dim 1]);    % Joint angular velocity
ddth = sym('ddth%d', [dim 1]); % Joint angular acceleration
c = sym('c%d', [1 dim]);        % Center of mass of each link
c = sym(c, 'real');
l = sym('l%d', [1 dim]);        % Length of each link
l = sym(l, 'real');
m = sym('m%d', [1 dim]);        % Mass of each link
m = sym(m, 'real');
I = sym('I%d', [1 dim]);        % Moment of inertia of each link
I = sym(I, 'real');
k = sym('k%d', [1 (dim-1)]);    % Stiffness of each joint
k = sym(k, 'real');
th0 = sym('th0%d', [1 dim]);    % Neutral position of each joint
th0 = sym(th0, 'real');
syms rou Cd1 Cd2 real
syms tau real

q = sym(zeros((dim+2),1));      % Generalized coordinates
dq = sym(zeros((dim+2),1));
ddq = sym(zeros((dim+2),1));

for i = 1:(dim+2)
    if i == 1
        q(i) = x;
        dq(i) = dx;
        ddq(i) = ddx;
    elseif i == 2
        q(i) = y;
        dq(i) = dy;
        ddq(i) = ddy;
    else
        q(i) = th(i-2);
        dq(i) = dth(i-2);
        ddq(i) = ddth(i-2);
    end
end

q = sym(q, 'real');
dq = sym(dq, 'real');
```

```
ddq = sym(ddq, 'real');

u = tau;      % Controls: Torque is applied at the joint between Link 1 and Link 2
p = [c l m I k th0 rou Cd1 Cd2];   % Parameters

ihat = [1; 0; 0];                          % x direction
jhat = [0; 1; 0];                          % y direction
khat = cross(ihat,jhat);                   % z direction
er = sym(zeros(3,1));                      % Direction along each link
ern = sym(zeros(3,1));                     % Direction perpendicular to each link

pos = sym(zeros(3,(dim+1)));               % Defining points: Beginning and end points of each
link
posM = sym(zeros(3,dim));                  % Midpoint of each link
posX = sym(zeros(3,dim, pts));             % Sample points along each link
pos(:,1) = x*ihat + y*jhat;                % Beginning point of Link 1

dr = sym(zeros(3,dim));                    % Velocity of defining points
ddr = sym(zeros(3,dim));                   % Acceleration of defining points
drX = sym(zeros(3,dim,pts));               % Velocity of sample points
ddrX = sym(zeros(3,dim,pts));              % Acceleration of sample points
drM = sym(zeros(3,dim));                   % Velocity of midpoints
ddrM = sym(zeros(3,dim));                  % Acceleration of midpoints

T = sym(zeros(dim,1));                     % Kinetic energy of each link
Ve = sym(zeros(dim-1,1));                  % Potential energy of each joint
P = sym(zeros(dim,1));                     % Power

Fx = sym(zeros(dim,pts));                  % Forces parallel to each link: Friction drag
Fy = sym(zeros(dim,pts));                  % Forces perpendicular to each link: Form drag +
added mass

% Generalized forces
Q_tau = M2Q(tau*khat,dth(2)*khat);         % Moment due to torque only
Q_F = 0;

R = sym(zeros((2*dim+2),1));

ddt = @(r) jacobian(r,[q;dq])*[dq;ddq];    % Function for taking time derivatives

F2Q = @(F,r) jacobian(r,q)'*(F);           % Force contributions to generalized forces
M2Q = @(M,w) jacobian(w,dq)'*(M);          % Moment contributions to generalized forces

% Symbolic Calculation
for i = 1:dim
    % Directions parallel the links
    er(:,i) = cos(sum(th(1:i)))*ihat + sin(sum(th(1:i)))*jhat;
    % Directions perpendicular to the links
    ern(:,i) = sin(sum(th(1:i)))*ihat + cos(sum(th(1:i)))*(-jhat);
    % End points
    pos(:,i+1) = pos(:,i) + l(i)*er(:,i);
    % Midpoints
    posM(:,i) = pos(:,i) + c(i)*er(:,i);
    % Velocity of defining points
```

```
    dr(:,i) = ddt(pos(:,i));
    % Acceleration of critical points
    ddr(:,i) = ddt(dr(:,i));
    % Velocity of midpoints of links
    drM(:,i) = ddt(posM(:,i));
    % Acceleration of midpoints of links
    ddrM(:,i) = ddt(drM(:,i));

    for j = 1:pts
        % Position of sample points
        posX(:,i,j) = pos(:,i) + (l(i)*(2*j-1)/(2*pts))*er(:,i);
        % Velocity of sample points
        drX(:,i,j) = ddt(posX(:,i,j));
        % Acceleration of sample points
        ddrX(:,i,j) = ddt(drX(:,i,j));
    end

    % Kinematic energy
    T(i) = (1/2)*m(i)*dot(drM(:,i),drM(:,i)) + (1/2)*I(i)*(sum(dth(1:i)))^2;
    % Potential energy
    if i < dim
        Ve(i) = (1/2)*k(i)*(th(i+1) - th0(i+1))^2;
    end

    % Hydrodynamic Forces
    [Fx(i,:), Fy(i,:), P(i)] = HydroForce(drX(:,i,:), ddrX(:,i,:), er(:,i), ern(:,i), rou, Cd1,
Cd2, l(i));
    % Generalized forces
    for j = 1:pts
        Q_F = Q_F + F2Q(Fx(i,j)*er(:,i),posX(:,i,j)) + F2Q(Fy(i,j)*ern(:,i),posX(:,i,j));
    end

    % Assemble R, the array of Cartesian coordinates of the key points
    R(2*i-1) = pos(1,i);
    R(2*i) = pos(2,i);
    if i == dim
        R(2*dim+1) = pos(1, dim+1);
        R(2*dim+2) = pos(2, dim+1);
    end
end

Tsum = sum(T);      % Total kinetic energy
Vsum = sum(Ve);     % Total potential energy

Q = Q_tau + Q_F;

% Derive Energy Function and Equations of Motion
E = Tsum + Vsum;
L = Tsum - Vsum;
Psum = sum(P) + tau*dth(2);

g = ddt(jacobian(L,dq)') - jacobian(L,q)' - Q;

% Rearrange Equations of Motion
```

```
A = jacobian(g,ddq);        % A should not contain any acceleration terms
b_subs = subs(A*ddq - g, [ddx; ddy; ddth], zeros(dim+2, 1));    % Manually set dd terms to be
zeros
% b = simplify(b_subs);
b = b_subs;

% Equations of Motion
Nz = length(dq)*2;
z(1:2:Nz,1) = q;
z(2:2:Nz,1) = dq;

% Generate functions (in Modeling folder)
matlabFunction(E,'file',['energy_' name],'vars',{z p}); % Energy
% matlabFunction(P,'file',['power_' name],'vars',{tau z p});  % Power
matlabFunction(R,'file',['z2R_' name],'vars',{z p});
matlabFunction(A,'file',['A_' name],'vars',{z p});
matlabFunction(b,'file',['b_' name],'vars',{z u p});
```

APPENDIX B

```
function [Fx1, Fy1, P1] = HydroForce(dr1, ddr1, er1, er1n, rou, Cd1, Cd2, l1)

dim = size(dr1);            % dim(3) = pts
vx1 = sym(zeros(1,dim(3))); % Velocity parallel to each link
vy1 = sym(zeros(1,dim(3))); % Velocity perpendicular to each link
ay1 = sym(zeros(1,dim(3))); % Acceleration perpendicular to each link
Fx1 = sym(zeros(1,dim(3))); % Forces parallel to each link: Friction drag
Fy1 = sym(zeros(1,dim(3))); % Forces perpendicular to each link: Form drag + added mass

for i = 1:dim(3)
    vx1(i) = dot(dr1(:,:,i),er1);
    vy1(i) = dot(dr1(:,:,i),er1n);
    ay1(i) = dot(ddr1(:,:,i),er1n);
    Fx1(i) = -1/2*rou*vx1(i)^2*Cd2*l1/dim(3)*sign(vx1(i));      % Forces parallel to links:
Friction drag
    Fy1(i) = -1/2*(rou*pi*(l1/dim(3))^2)*ay1(i) -1/2*rou*vy1(i)^2*Cd1*l1/dim(3)*sign(vy1(i)); %
Forces perpendicular to each link: Form drag + added mass
end

P1 = Fx1.*vx1 + Fy1.*vy1;   % Power
```

APPENDIX C

```
close all;
clear all;
clc;

global dim

dim = 5;

% Positions of centers of mass
c = [0.05 0.025*ones([1 (dim-1)])];     % [m]
% Link lengths
l = [0.1 0.05*ones([1 (dim-1)])];       % [m]
% Radii of cross-sections of links
r = [0.01 0.01*ones([1 (dim-1)])];      % [m]
% Masses
% Density of Vytaflex ~= 1000 kg/m^3
m = [2 0.1*ones([1 (dim-1)])];          % [kg]
% Inertia: moment of inertia of a rod: 1/12*m*l^2
I = 1/12.*m.*l.^2;                      % [kg*m^2]
% Joint stiffness
k = [0 0.09 0.05 0.01];
% k = [0 0.09 0.05 0.03];
% Initial angles
th0 = zeros([1 dim]);                   % [m]
% Lift and drag forces
rou = 1000;     % [kg/m^3], 1000
Cd1 = 0;       % [dimensionless], perpendicular to links
Cd2 = 0;       % [dimensionless], parallel to links
Ad = 0;         % [m^2]
Al = 0.5;       % [m^2]

p = [c l r m I k th0 rou Cd1 Cd2 Ad Al];  % Parameters
z0 = zeros([(dim+2)*2 1]);
tspan = [0 10];
aSpeed = 1;   % Animation speed. aSpeed = 1 => real time
opts = odeset('AbsTol',1e-3,'RelTol',1e-3);     % Orginal tolerance 1e-10

f = @(t,z) dynamics(t,z,p);
sol = ode45(f,tspan,z0,opts);

% Animation
R = z2R_ThreeLink(sol.y,p);
t = sol.x;
C = zeros(dim, 2);
for i = 1:dim
    C(i,:) = [i i+1];
end
animate(t,R,C,aSpeed)
```

APPENDIX D

```
function dz = dynamics(t,z,p)

global dim  u

torq = 0.05;

th1 = z(5);
dth1 = z(6);
th2 = z(7);
dth2 = z(8);

n = 6;

if t <= 0.01
    u = torq;
end
if (th2-th1) > pi/n && (dth2-dth1) >= 0
    u = -torq;  % [Nm]
elseif (th2-th1) < -pi/n && (dth2-dth1) <= 0
    u = torq;   % [Nm]
end

A = A_ThreeLink(z,p);        % get the full A matrix
b = b_ThreeLink(z,u,p);       % get the full b vector

x = A\b;                     % solve system for accelerations (and possibly contact forces)
dz(1:2:((dim+2)*2-1),1) = z(2:2:((dim+2)*2),1);   % set speeds
dz(2:2:((dim+2)*2)) = x(1:(dim+2));               % set accelerations

end
```

APPENDIX E

```
close all;
clear all;
clc;

list_of_files = dir([fullfile(pwd) '\\*.xlsx']);        % Load all the files
num = length(list_of_files);                            % 28 files in total
DelCol = [1 3 5 7];                                     % Delete column 1, 3, 5, 7
mass = 885/1000;                                        % Total mass = 885 g
g = 9.81;                                               % Gravitational acceleration = 9.81 m/s^2

for i = 1:num
    fileName = list_of_files(i).name;                   % Obtain file name
    expData = strrep(fileName, ' ','_');                % Replace space with underscore
    expData = strcat('exp_', expData);                  % Add 'exp_'in front of the file name
    expData = expData(1:end-5);                         % Get rid of file extension .xlsx
    exp{i} = expData;                                   % Store variable name
    plotName{i} = fileName(1:end-5);                    % Store plot name

    temp = xlsread(fileName);                           % Load data from corresponding spreadsheet
    temp(:,DelCol) = [];                                % Delete column 1, 3, 5, 7
    temp(:,4) = (temp(:,4) - temp(1,4))/1000;           % Normalize time
    temp(:,2) = (temp(:,2) - temp(end,2))/1000;         % Normalize distance
    [maxCurr, ind] = max(temp(:,1));                    % Find the peak current and index
    start = ind + 65;                                   % New start point of useful data
    temp = temp(start:end, :);                          % Eliminate transient phase
    temp(:,2) = -temp(:,2) + max(temp(:,2));            % Flip distance measurement (start with zero)
    temp(:,4) = temp(:,4) - min(temp(:,4));             % Zero the start point of time
    eval(sprintf('%s = temp;', exp{i}));                % Load data into corresponding variable
    time = temp(:,4);                                   % Time
    current = temp(:,1);                                % Current
    dist = temp(:,2);                                   % Distance

    data.avgCurr(1,i) = mean(current);                  % Record average current for this experiment
    time2(:,1) = time;                                  % Create a time array for least-square analysis
    time2(:,2) = ones(length(time),1);
    x = lscov(time2, dist);                             % Least-square analysis to get slope
    data.avgVel(1,i) = x(1);                            % Record average velocity for this experiment

    % Compute Cost of Transport
    data.vol(1,i) = str2double(strtok(fileName, 'V')); % Obtain voltage corresponding to this
experiment
    data.CoT(1,i) = data.vol(1,i)*data.avgCurr(1,i)/(mass*g*data.avgVel(1,i));  % Compute Cost of
Transport

    % Plot average distance and current data
    figure(3)
    if i <= 4                    % 10 V
        plot(data.avgCurr(1,i), data.avgVel(1,i), 'o','Color',[rand(),rand(),1]);
    elseif i > 4 && i <= 8       % 15 V
        plot(data.avgCurr(1,i), data.avgVel(1,i), '*','Color',[rand(),0.5,rand()]);
    elseif i > 8 && i <= 12      % 20 V
```

```
        plot(data.avgCurr(1,i), data.avgVel(1,i), '+','Color',[rand(),rand(),0.5]);
    elseif i > 12 && i <= 16    % 25 V
        plot(data.avgCurr(1,i), data.avgVel(1,i), 'x','Color',[rand(),0.7,rand()]);
    else                        % 5V
        plot(data.avgCurr(1,i), data.avgVel(1,i), '^','Color',[rand(),0.2,rand()]);
    end
    hold on;

    clearvars time2
end

    % Summary Plot: Speed vs. Current
    data.name = exp;
    labels = plotName;
    figure(3)
    text(data.avgCurr(1,:), data.avgVel(1,:), labels, 'VerticalAlignment','bottom',
'HorizontalAlignment','center','FontSize',12)
    xlabel('Average Current [A]', 'FontSize',12);
    ylabel('Average Speed [m/s]','FontSize',12);
    legend(plotName);

    % Cost of Transport
    figure(4)
    plot(data.vol(1,:), data.CoT(1,:), 'o');
    xlabel('Voltage [V]', 'FontSize',12);
    ylabel('Cost of Transport', 'FontSize',12);
    text(data.vol(1,:), data.CoT(1,:), labels, 'VerticalAlignment','bottom',
'HorizontalAlignment','center','FontSize',12)
    xlim([2.5 27.5]);
```

APPENDIX F

```
close all;
clear all;
clc;

n = 100;
Coupler = linspace(2,50,n);   % [mm]
Rocker = 9;     % [mm]
Crank = 5;      % [mm]
Base = linspace(20,30,n);      % [mm]

l2 = Rocker;
l3 = Crank;
RockerRange = zeros(n,n);

for i = 1:n
    l4 = Coupler(i);
    for j = 1:n
        l1 = Base(j);
        if ((l1 + l3) < (l2 + l4)) && ((l1 + l2) > (l3 + l4)) && ((l1 + l2) > (l4 - l3)) && (l4 >
l3)
            aMax = acos(((l3 + l4)^2 - (l1^2 + l2^2))/(-2*l1*l2));   % [rad]
            aMin = acos(((l4 - l3)^2 - (l1^2 + l2^2))/(-2*l1*l2));   % [rad]
            RockerRange(i,j) = (aMax - aMin)/2*(180/pi);
            if isreal(RockerRange(i,j)) == 0
                RockerRange(i,j) = 0;
            end
        else
            RockerRange(i,j) = 0;
        end
    end
end

newRange = RockerRange(RockerRange~=0);
minRange = min(newRange)
[row, col] = find(RockerRange == minRange);
A = [Crank Rocker Coupler(row) Base(col)];

figure(1)
surf(Coupler, Base, RockerRange);
xlabel('Coupler [mm]');
ylabel('Base [mm]');
zlabel('RockerRange [deg]');
```